Dynein-Mediated Regional Cell Division Reorientation Shapes a Tailbud Embryo.

Article

Dynein-Mediated Regional Cell Division Reorientation Shapes a Tailbud Embryo

Ayaki Nakamoto,
Gaku Kumano

ayaki.nakamoto.a4@tohoku.
ac.jp

HIGHLIGHTS

Differently oriented cell division creates epithelial bending to shape the tail bud

Epidermal cells divide in different orientations in two different adjacent regions

Posterior cells undergo dynein-dependent spindle rotation and divide along A-P axis

Dynein is enriched in the anterior surface of the posterior cells

Article

Dynein-Mediated Regional Cell Division Reorientation Shapes a Tailbud Embryo

Ayaki Nakamoto[1,2,*] and Gaku Kumano[1]

SUMMARY

Regulation of cell division orientation controls the spatial distribution of cells during development and is essential for one-directional tissue transformation, such as elongation. However, little is known about whether it plays a role in other types of tissue morphogenesis. Using an ascidian *Halocynthia roretzi*, we found that differently oriented cell divisions in the epidermis of the future trunk (anterior) and tail (posterior) regions create an hourglass-like epithelial bending between the two regions to shape the tailbud embryo. Our results show that posterior epidermal cells are polarized with dynein protein anteriorly localized, undergo dynein-dependent spindle rotation, and divide along the antero-posterior axis. This cell division facilitates constriction around the embryo's circumference only in the posterior region and epithelial bending formation. Our findings, therefore, provide an important insight into the role of oriented cell division in tissue morphogenesis.

INTRODUCTION

During animal development, tissues, organs, and organisms are shaped into specific structures. Elucidating the mechanisms of these dynamic processes at multiple levels—molecules, cells, tissues, and organisms—is an important and fundamental issue in developmental biology. Although the structures of animals show considerable variation in shape, recent research has demonstrated the involvement of some fundamental mechanisms in the process of creating tissues, organs, and organisms across animal species. An example of this is epithelial bending or invagination, which is found in several cell morphogenetic events including gastrulation in *Drosophila*, *Xenopus*, and sea urchin (Sawyer et al., 2010; Davidson, 2012), and formation of the tracheal system, dorsal transverse fold, and leg epithelial fold in *Drosophila* embryos (Kondo and Hayashi, 2013; Wang et al., 2012; Ambrosini et al., 2019). However, interestingly, studies have shown that epithelial bending is driven by different cellular mechanisms, including apical constriction (Sawyer et al., 2010; Martin and Goldstein, 2014), mitotic cell rounding (Kondo and Hayashi, 2013), differential positioning of adherence junctions (Wang et al., 2012), and an actomyosin structure connecting the apical surface to the nucleus, which is anchored to the basal side in apoptotic cells (Ambrosini et al., 2019).

Regulation of cell division orientation, a well-known mechanism for proper distribution of determinants during asymmetric cell divisions (Bergstralh et al., 2017; di Pietro et al., 2016), is also essential for tissue morphogenesis such as tissue elongation and thickening (Panousopoulou and Green, 2014; da Silva and Vincent, 2007; Lechler and Fuchs, 2005). This is achieved via controlling the organized spatial distribution of cells following the oriented cell divisions. Three main rules apply to regulation of cell division orientation. The first is the Hertwig's rule, wherein cells divide along the longest axis of the cell; this is frequently observed in epithelial cell divisions (Hertwig, 1884; Brun-Usan et al., 2017; Minc et al., 2011; Minc and Piel, 2012). The second is the Sachs' rule (Saches, 1878), typically found in early embryonic cell divisions during cleavage stages (Guerrier, 1970; Meshcheryakov and Beloussov, 1975), wherein cells divide in a direction perpendicular to the orientation of the previous division. The third is the cell polarization rule (Brun-Usan et al., 2017; Morin and Bellaïche, 2011), wherein cells are polarized either by external cues or localized intrinsic factors and divide according to the polarity. One of the molecular bases of such cell polarization is the core cortical machinery that orients mitotic spindles and is known to function in asymmetric cell divisions, including those of *Drosophila* neuroblasts (di Pietro et al., 2016) and the *Caenorhabditis elegans* P1 cell of the two-cell embryo (Grill and Hyman, 2005; Rose and Gönczy, 2014). The core machinery comprises Mud, Pins, and Gαi in *Drosophila* (Bowman et al., 2006; Schaefer et al., 2000); LIN-5, GPR1/2, and GOA-1/GPA-16 in *C. elegans* (Srinivasan et al., 2003; Colombo et al., 2003); and NuMA, LGN, and Gαi in vertebrates (Du and Macara, 2004; Peyre et al., 2011). These proteins form a complex with the dynein motor at the cell cortex, thereby exerting a pulling force on the astral microtubules by moving along them until the spindle is properly aligned (di Pietro et al., 2016; Bergstralh et al., 2017).

[1]Asamushi Research Center for Marine Biology, Graduate School of Life Sciences, Tohoku University, 9 Sakamoto, Asamushi, Aomori 039-3501, Japan

[2]Lead Contact

*Correspondence: ayaki.nakamoto.a4@tohoku. ac.jp

A

A1 NR+1 h A2 NR+1 h 30min A3 NR+2 h A4 NR+2 h 45 min

Trunk Tail Trunk Tail

Anterior Posterior

A1' A2' A3' A4'

B

B1 B2 B3 Anterior

Anterior Posterior

Anterior Posterior Posterior

10/11 17/19

C

0 min 2 min 4 min

X-Z section

Anterior Posterior X-Y plane: lateral view of the embryo

6 min 8 min 10 min

X-Z section

X-Y plane: lateral view of the embryo

11/11

D

control 20 mM HU 50 mM HU 100 mM HU
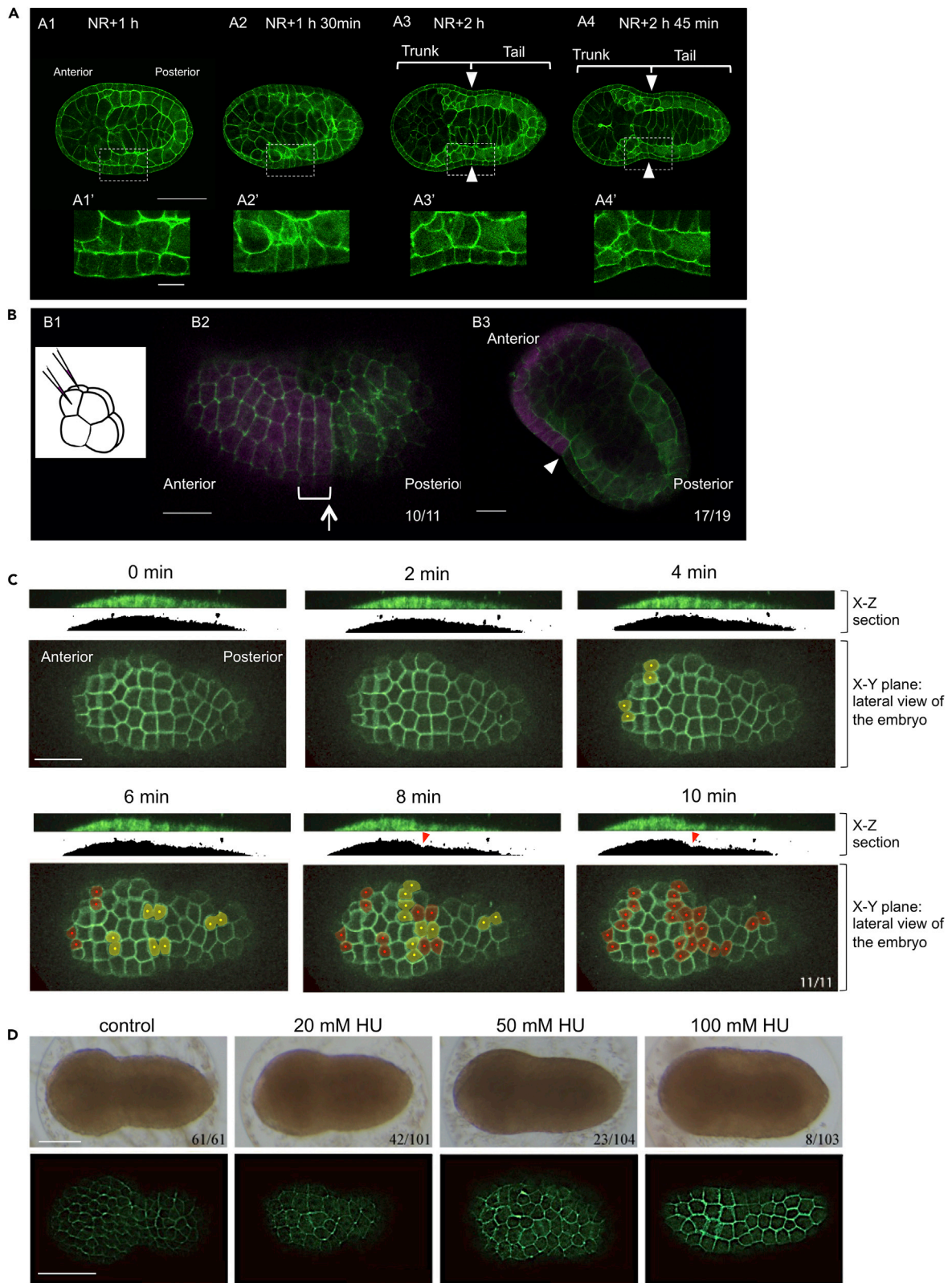
61/61 42/101 23/104 8/103

Figure 1. Epithelial Bending Formation and Tailbud Shaping

(A) Phallacidin-stained embryos at the neurula through early tailbud stages. The image of each stage is a single focal plane, where the area of the embryo is at maximum. A1–A4 are viewed with anterior to the left. Close-up views of the dot-lined square in A1–A4 are shown at the bottom (A1'–A4'). (A1) At 1 h after the neurula rotation (NR+1 h) (Nishide et al., 2012), approximately 30 min before the start of the 11th epidermal cell divisions. (A2) At 1 h and 30 min after the neurula rotation (NR+1 h 30 min). (A3) 2 h after the neurula rotation (NR+2 h). (A4) 2 h and 45 min after the neurula rotation (NR+2 h 45 min). Arrowheads in A3 and A4 indicate the boundary between the trunk and tail regions. Scale bars, 100 μm (A1–A4), 20 μm (A1'–A4').

(B1) Schematic diagram of eight-cell embryo injected for lineage trace. Lateral view, with anterior to the left. Fluorescent dye was microinjected into anterior ectodermal cells, named a4.2 cells, on both sides of the embryo. (B2) The descendants of a4.2 cells (magenta). Cell shape is visualized with Phallacidin (green). The boundary of anterior and posterior ectodermal lineages is indicated by an arrow. Rows of rectangular-shaped cells are indicated with white brackets. The digits in the bottom right-hand corner indicate the proportion of the embryo in which rows of rectangular-shaped cells were derived from a4.2 cells. Scale bar, 50 μm. (B3) Frontal section of an early tailbud embryo. The descendants of a4.2 cells (magenta), and cell shape is visualized with Phallacidin (green). The deepest position of the epithelial bending is indicated by an arrowhead. The digits in the bottom right-hand corner indicate the proportion of the embryo in which the lineage boundary corresponded to the deepest position of the epithelial bending. Scale bar, 50 μm.

(C) Snap shot images obtained from live confocal imaging showing the epidermal cell division. The cell membrane was labeled with PH-YFP. Anterior is to the left. In each time point, a section along the anterior–posterior axis (top, X–Z section) and lateral view of the embryo (bottom, X–Y section) are shown. Shadow images of the X–Z section are shown for clarification of the formation of epithelial bending (red arrowheads). The dividing and divided cells in the X–Y plane are indicated with yellow and red dots, respectively. The digits in the bottom right-hand corner at the 10 min image indicate the proportion of the embryo in which epidermal cell division accompanied formation of epithelial bending. Scale bar, 100 μm.

(D) Hydroxyurea (HU) treatment. The effect of HU on epidermal cell division (bottom) and formation of epithelial bending (top). The treated embryos were fixed and stained with Phallacidin. The number of embryos that form epithelial bending is shown in the bottom right. Scale bars, 100 μm.

Ascidians are marine invertebrates that belong to the phylum Chordata. They are useful model systems for studying cellular behavior during morphogenesis in embryonic stages because of their invariant cell lineage and small number of cells constituting the embryo (Conklin, 1905; Nishida, 1986; Kumano and Nishida, 2007; Ogura and Sasakura, 2013). One remarkable morphogenetic process during ascidian embryogenesis, in addition to neural tube closure (Hashimoto et al., 2015) and endoderm invagination during gastrulation (Sherrard et al., 2010), is tail formation. In transitioning from the neurula to tailbud stages, a boundary between the future trunk and tail regions appears morphologically as an hourglass-like epithelial bending at the middle level of the embryo along the anteroposterior (A–P) axis (Hotta et al., 2007, Figure 1A). Following this, the tail region undergoes extensive elongation along the A–P axis (Hotta et al., 2007, Figure 1A). This derives mainly from cell rearrangements (Munro and Odell, 2002a, 2002b; Passamaneck et al., 2007), rather than cell proliferation, and the tail region ends up being several times longer than is the trunk region. This is in contrast with other animals including some annelid and vertebrate species, in which tail formation depends on proliferation of a small group of cells known as posterior growth zones or tailbuds, which are located at the posterior end of the embryo (Williams and Nagy, 2017; McGrew et al., 2008).

In this study, we analyzed the molecular and cellular mechanisms that shape the tailbud embryo of the ascidian *Halocynthia roretzi*. We propose a model for epithelial bending and overall body shape mechanisms that require cell divisions oriented perpendicularly to each other in two different adjacent areas of the epithelial layer. We determined that epidermal cells in the anterior and future trunk region divided around the circumference of the embryo, whereas those in the posterior and future tail region divided along the A–P axis. We also found that the difference in division orientation between the anterior and posterior regions was established by dynein-mediated spindle rotation just before the cell divisions in the posterior cells, which resulted in its orientation along the A–P axis regardless of cell shape. Accordingly, this cell division results in constriction around the circumference of the embryo only in the posterior region and creates epithelial bending at the boundary of the anterior and posterior regions to shape the tailbud.

RESULTS

Cell Morphology around the Future Epithelial Bending Site

To understand the cellular mechanisms by which the hourglass-like epithelial bending to shape the *H. roretzi* tailbud embryo is generated on the lateral side of the neurula embryo (Figure 1A), our first aim was to characterize the morphology of epidermal cells in the outermost and epithelial layer of the embryo during bending formation. Phallacidin staining of fixed neurula embryos revealed that epidermal cells around the future bending region exhibit rectangular shape, frequently arranged in two rows, with their long axes aligned around the circumference of the embryo (bracket in Figure 1B2). Cell lineage analyses, in which descendants of the anterior ectodermal cells named a4.2 were traced following injection of pairs of a4.2 cells with a fluorescent dye, Texas Red dextran, at the eight-cell stage (Figure 1B1), revealed that the ectodermal A–P lineage boundary, which is defined by the second cleavage after fertilization, coincides
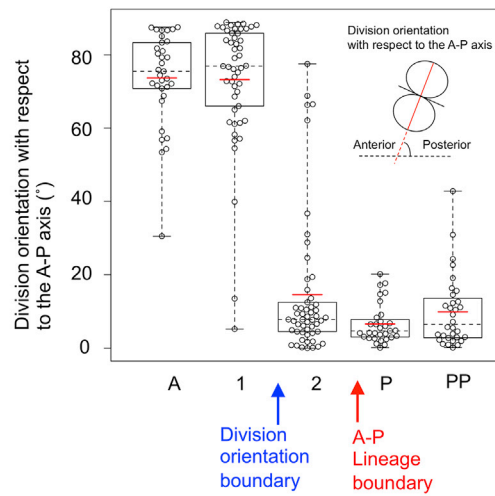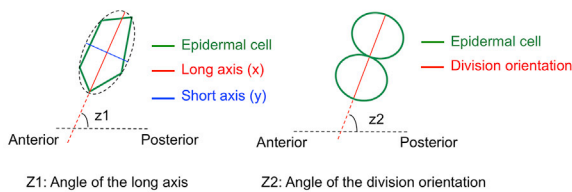
A

B

Anterior — Posterior

Division orientation boundary

A-P Lineage boundary

C
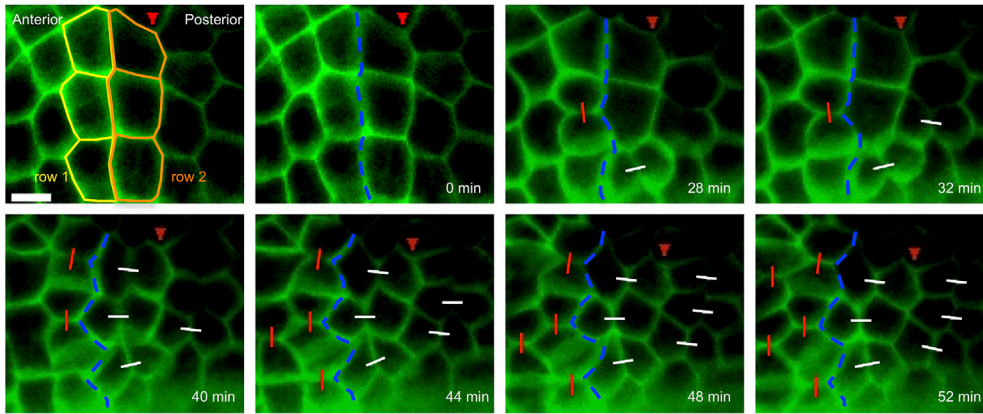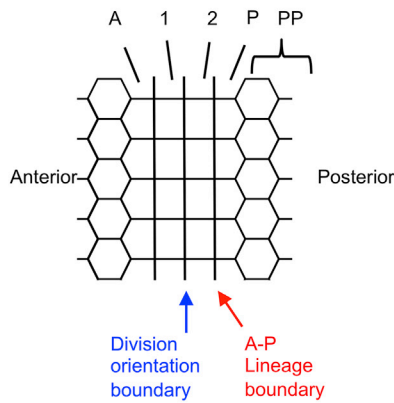
Division orientation with respect to the A-P axis in each cell row

Division orientation boundary

A-P Lineage boundary

D

Z1: Angle of the long axis

Z2: Angle of the division orientation

	long axis(x) / short axis (y)	angles of long axis with respect to the A-P axis (z1)
row 1	1.58 (s.d.=0.27)	81.7˚ (s.d.=8.64)
row 2	1.60 (s.d.=0.30)	81.4˚ (s.d.=6.76)
	p>0.45 (U-test)	P>0.45 (U-test)

E

Angles of the long axis (z1) and division orientation (z2) in each cell row
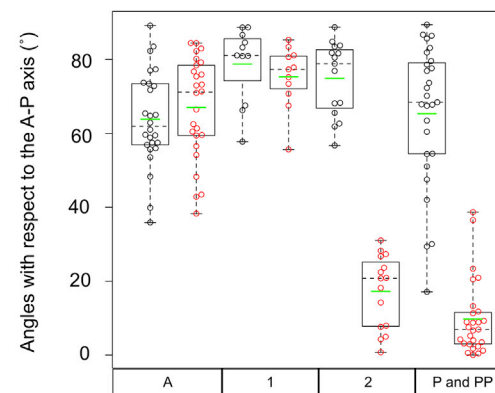
o Angles of the long axis (z1)
o Angles of the division orientation (z2)

Figure 2. Differently Oriented Cell Division with Clear Boundary

(A) Snap shot images from Video S1 showing the epidermal cells. Lateral side view. In the top left image, cell rows 1 and 2 (see below for the definition) are indicated by yellow and orange lines, respectively. The boundary of the anterior and posterior ectodermal lineages is indicated by red arrowhead. Division orientation boundary is indicated by blue broken lines. Division angles with respect to the A–P axis are indicated by white line (between 0° and 30°) and red line (between 61° and 90°). Sister cells are connected with white line and red line according to the division angles. Scale bar, 20 μm.

(B) Schematic diagram of epidermal cells on the lateral side of the embryo. The cell row located anterior to the division orientation boundary is indicated as row 1, that posterior to row 1 is indicated as row 2, that anterior to row 1 is indicated as row A, that posterior to row 2 is indicated as row P, and that posterior to row P is indicated as row PP.

(C) Division orientation with respect to the A–P axis. The inset in the graph demonstrates how to measure the angle of division orientation with respect to the A–P axis. Each circle represents a measurement of a single cell. The values were extracted from 41 cells/8 embryos for row A, 58 cells/9 embryos for row 1, 62 cells/9 embryos for row 2, 41 cells/6 embryos for row P, and 23 cells/3 embryos for row PP. Data are represented as individual values and boxplots. Means are indicated as red horizontal bars. Medians are indicated with dashed lines. Boxes indicate second and third quartiles, and whiskers indicate the maximum and minimum values.

(D) Schematic diagrams showing how the angles of the cell long axis (z1) and the division orientation axis (z2) are defined with respect to the A–P axis. At the bottom is a table describing the ratio of the long to the short axes (x/y) and the angle of the long axis of epidermal cells in rows 1 and 2 with respect to the A–P axis to evaluate cell geometry.

(E) The values of z1 (black circle) and z2 (red circle) were extracted from 26 cells/5 embryos for row A, 11 cells/6 embryos for row 1, 15 cells/6 embryos for row 2, and 27 cells/3 embryos for rows P and PP. Data are represented as individual values and boxplots. Means are indicated as green horizontal bars. Medians are indicated with dashed lines. Boxes indicate second and third quartiles, and whiskers indicate the maximum and minimum values.

both with the posterior end of the rows of rectangular-shaped cells (90.9% [n = 11], arrow in Figure 1B2) and with the deepest point of the epithelial bending (89.5% [n = 19], arrowhead in Figure 1B3) following its formation.

## Epidermal Cell Divisions during Epithelial Bending and Tailbud Shape Formation

We next carried out live-imaging analysis using PH-YFP encoding a fusion YFP fluorescent protein to a pleckstrin homology (PH) domain to visualize cell membranes (Tall et al., 2000; Passamaneck et al., 2007) of epidermal cells on the lateral side of the embryo. We found that the timing of the formation of epithelial bending (X-Z sections in Figure 1C) coincides with the timing of epidermal cell divisions (X-Y planes in Figure 1C). These cell divisions were the 11th to occur after fertilization (Figure S1). To examine whether the epidermal cell divisions are related causally to the formation of epithelial bending, we cultured embryos in the presence of Hydroxyurea (HU), a cell division inhibitor, beginning at approximately 1 h and 30 min prior to the cell divisions. We found that HU treatment inhibited both cell division (bottom in Figure 1D) and formation of epithelial bending/tailbud shaping (top in Figure 1D) in a concentration-dependent manner. However, we cannot rule out the possibility that the resultant larger cell size itself might have blocked the morphogenesis. We also cannot eliminate the possibility that this treatment affects other cells, especially those located inside the embryo; however, previous studies suggest that at least notochord and muscle cells, which constitute a large portion of the tail region, have already ceased their embryonic cell divisions before the late neurula stage (Nishida, 1987; Kuwajima et al., 2014).

Differently Oriented Cell Divisions between Anterior and Posterior Regions

We then tried to clarify the potential contribution of those epidermal cell divisions to the formation of epithelial bending and the tailbud shaping. Via live-imaging analysis with PH-YFP, we found that epidermal cells undergo differently oriented cell divisions in anterior and posterior regions on the lateral side of the embryo. Cells in the anterior region divide around the circumference of the embryo (red lines in Figure 2A), whereas cells in the posterior region divide along the A–P axis (white lines in Figure 2A), forming a clear boundary of division orientation around the bending forming region (Figure 2A, Video S1). To ascertain the precise location of the division orientation boundary, we took advantage of asymmetric inheritance of the injected mRNA and identified the ectodermal A–P lineage boundary by means of different cell membrane fluorescence intensity. We ascertained that the division orientation boundary is located one cell row anterior to the A–P lineage boundary and that the one cell row difference was invariant in nearly all the embryos observed (Figures 2B and 2C).

Comparison of division orientations between different rows of the rectangular-shaped cells (rows 1 and 2 in Figures 2A and 2B) is especially interesting as they divided in directions nearly perpendicular to each other (red circles in the middle two columns of Figure 2E), even though their cell geometries are almost identical in terms of cell shape and long axis orientation (Figure 2D, black circles in the middle two columns of Figure 2E). The cells in row 1 divided along their long axes, whereas those in row 2 did not (Figure 2E). Our analyses of other cells also revealed that epidermal cells in a row anterior to row 1 (row A in Figure 2B) divide
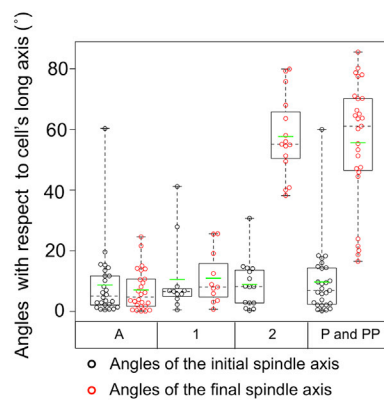
A rows 1 and 2

B rows P and PP

C

○ Angles of the initial spindle axis
○ Angles of the final spindle axis

D
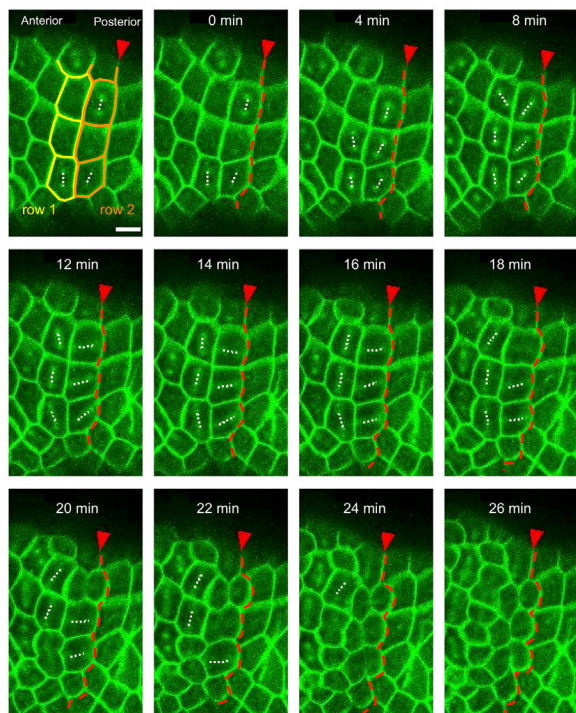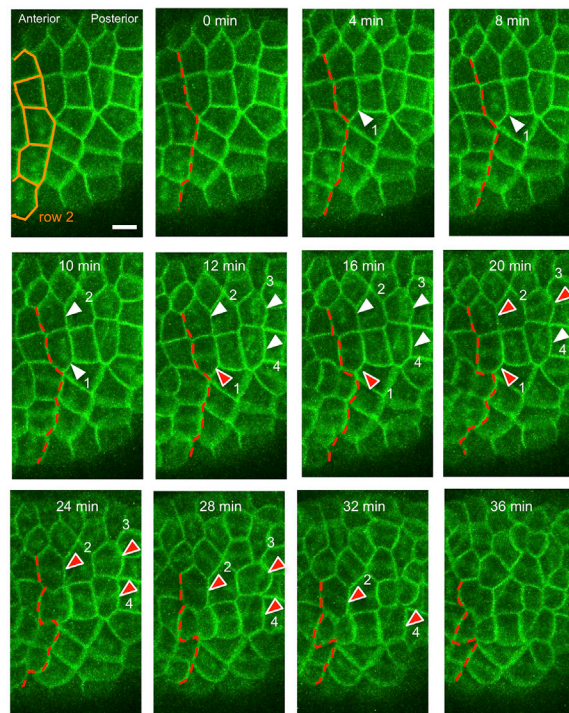
Direction of spindle rotation and cell geometry

| | | Z1 | | Z1 |
		Anterior	Posterior	Anterior	Posterior
Angles of the long axis (z1)		Z1< 90° (n=19)		Z1> 90° (n=19)
Direction of Spindle rotation when viewed from apical side	Clockwise	14		4
	Counter Clockwise	5		15

E

Boundary of A-P lineage

Boundary of A-P lineage and the deepest position of the bending

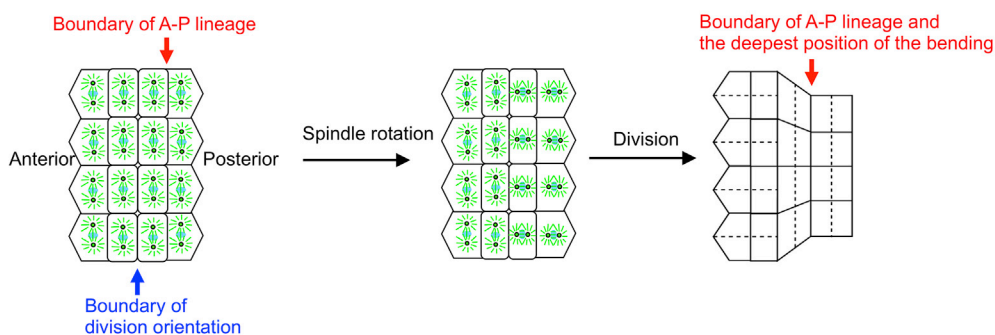Anterior → Spindle rotation → Division → Posterior

Boundary of division orientation

Figure 3. Spindle Rotation before the Epidermal Cell Division

(A) Snap shot images from Video S2 showing the spindle orientation in rows 1 and 2. In the top left image, cell rows 1 and 2 are indicated by yellow and orange lines, respectively. Anterior is to the left, and the lineage boundary is indicated by red arrowhead and red broken lines. Orientation of the spindle is indicated with dotted white lines. 0 min indicates the start of the observation.

(B) Snap shot images from Video S3 showing the spindle rotation in rows P and PP. In the top left image, cell row 2 is indicated by orange line. Anterior is to the left, and the lineage boundary is indicated by red broken lines. Note that the lineage boundary becomes zigzag due to different cell division timing during the cell division period. 0 min indicates the start of the observation. White arrowheads indicate that the spindle is aligned along the circumference of the embryo, whereas red arrowheads indicate that the spindle is either rotating or aligned along the A–P axis. Scale bar, 20 μm (A and B).

(C) The angle of the spindle axis with respect to cell's long axis. Black circles and red circles indicate the initial and final angles, respectively. The values were extracted from 26 cells/5 embryos for row A, 11 cells/6 embryos for row 1, 15 cells/6 embryos for row 2, and 27 cells/3 embryos for rows P and PP. Data are represented as individual values and boxplots. Means are indicated as green horizontal bars. Medians are indicated with dashed lines. Boxes indicate second and third quartiles, and whiskers indicate the maximum and minimum values.

(D) Direction of spindle rotation in two cases: one is when the angle of the long axis was less than 90° (left); the other is when the angle was more than 90° (right).

(E) A model for the formation of epithelial bending during the 11th epidermal cell division. Mitotic spindle rotations in rows 2 and P create perpendicularly oriented cell division between the anterior and posterior regions and contribute to the formation of epithelial bending (see text for detail).

along their long axes (left-most column of Figure 2E), whereas epidermal cells in rows posterior to row 2 (rows P and PP in Figure 2B) do not (right-most column of Figure 2E). These findings suggest that cells in rows 2, P, and PP undergo cell divisions against the Hertwig's rule (Hertwig, 1884) and that a mechanism actively directs their division orientation so that they divide along the A–P axis.

## Mitotic Spindle Rotation in Posterior Epidermal Cells

We next investigated how epidermal cells in the posterior region come to divide along the A–P axis. We conducted live-imaging analysis using MAP7-GFP, which is known to localize to the microtubules and spindle poles during mitosis (McDougall et al., 2015), together with PH-YFP, to visualize mitotic spindle orientation in epidermal cells. We found that the epidermal cells in rows 2, P, and PP undergo mitotic spindle rotation such that the spindles are oriented along the A–P axis before cell divisions (Figures 3A and 3B; Videos S2 and S3). In contrast, the spindles of the cells in row 1 remained oriented in the same direction and did not rotate (Figure 3A; Video S2). Notably, the mitotic spindles were aligned along the long axes of the cells prior to rotation (Figures 3A–3C). The spindles then rotated in either a clockwise or counterclockwise direction, with most of them achieving the reorientation via the shorter of the two rotation paths (76.3% [n = 38], Figure 3D).

Based on the above findings, we propose a model for the hourglass-like epithelial bending formation to shape the tailbud embryo of the ascidian *H. roretzi* (Figure 3E). Epidermal cells on the lateral side of the neurula embryo divide in a different orientation perpendicular to each other in the anterior and posterior regions after the collective and regional rotation of mitotic spindles in the posterior cells. This cell division with different division orientation facilitates constriction around the embryo's circumference only in the posterior region, with a lesser number of daughter cells distributed around the circumference than in the anterior region, which leads to the generation of a bending at the boundary between the anterior and posterior regions.

Dynein-Mediated Mitotic Spindle Rotation and Tailbud Shape Formation

To evaluate our model, we tried to disrupt the mitotic spindle rotation pharmacologically and ascertain its effect on the formation of a thinner and longer posterior body part and epithelial bending for the tail bud shaping. Research has shown that a motor protein dynein localizes at a cell cortex and drives mitotic spindle rotation for determination of cell division orientation (Lu and Johnston, 2013; di Pietro et al., 2016). Therefore, we treated embryos with 30 μM of a dynein inhibitor, Ciliobrevin D (Firestone et al., 2012; Lecland and Lüders, 2014), for 1 h before the 11th ectodermal cell divisions. This abrogated the division orientation of the epidermal cells in rows 2, P, and PP and directed it in a more circumferential direction, increasing the angles with respect to the A–P axis when compared with control cells treated with DMSO (Figures 4A–4C; Videos S4 and S5). The division angles of the cells treated with Ciliobrevin D, especially those in rows P and PP, were distributed relatively evenly in a wide range between 0° and 90° (Figure 4C); this is likely because the angles of the cells' long axes in rows P and PP were distributed in a similar way (Figure 2E), along which the mitotic spindles were aligned originally (Figure 3C), and they divided according to Hertwig's rule. Intriguingly, the inhibitor-treated embryos did not have the normal shape of tailbud embryos and instead displayed a significantly reduced extent of epithelial bending, as evaluated using two
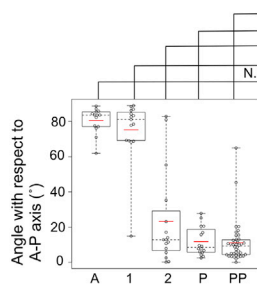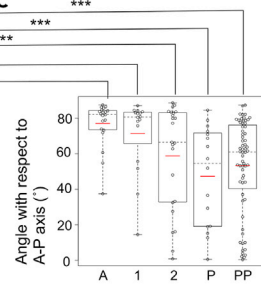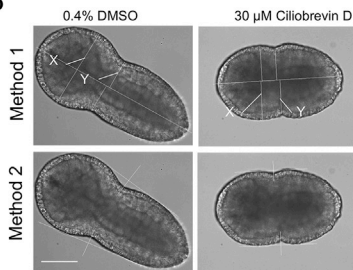
A 0.4% DMSO
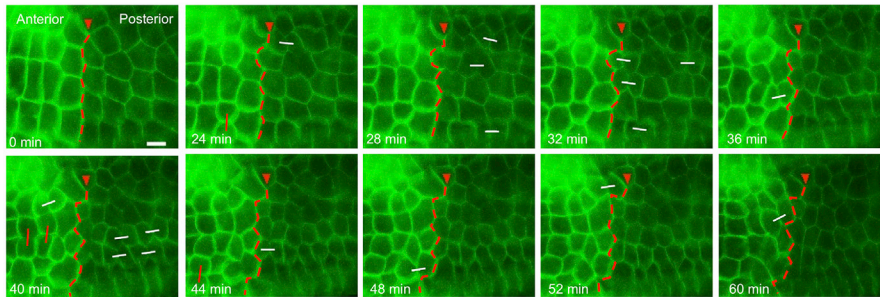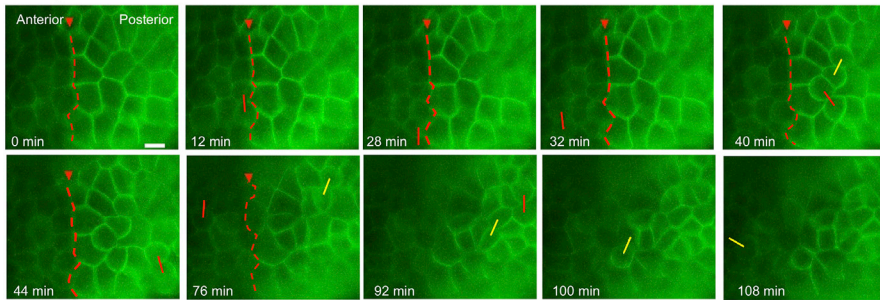
B **C**

Division angle of each cell row in the embryos treated with 0.4% DMSO (n=5 embryos)

Division angle of each cell row in the embryos treated with 30 μM Ciliobrevin D (n=7 embryos)

D

Method 1	Y/X
0.4% DMSO (n=10)	0.77 (s.d. =0.036)
30 μM Ciliobrevin D (n=19)	0.90 (s.d.=0.032)

***

Method 2	Depth of bending
0.4% DMSO (n=10)	16.69 μm (s.d.=3.37)
30 μM Ciliobrevin D (n=19)	8.18 μm (s.d.=3.42)

***

E

0.4 % DMSO

Trunk width (n=10)	214.4 μm (s.d. =8.73)
Tail width (n=10)	180.6 μm (s.d.=7.47)
Tail length (n=10)	237.7 μm (s.d.=10.45)

30 μM Ciliobrevin D

Trunk width (n=19)	232.3 μm (s.d. =13.37)
Tail width (n=19)	214.7 μm (s.d.=8.83)
Tail length (n=19)	180.8 μm (s.d.=9.83)

F

Before bending

a. Trunk width (n=11)	224.0 μm (s.d. =2.22)
b. Tail width (n=11)	220.7 μm (s.d. =2.72)
c. Tail length (n=11)	170.5 μm (s.d.=7.62)

After bending

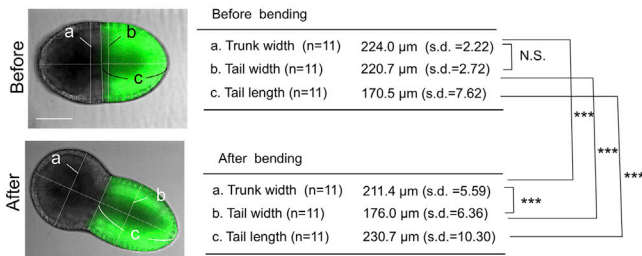|	
a. Trunk width (n=11)	211.4 μm (s.d. =5.59)
b. Tail width (n=11)	176.0 μm (s.d.=6.36)
c. Tail length (n=11)	230.7 μm (s.d.=10.30)

Figure 4. Disruption of the Orientation of Epidermal Cell Division and Epithelial Bending by Treatment with Dynein Inhibitor

(A) Division pattern of epidermal cells in the control embryo and embryo treated with Ciliobrevin D. Lineage boundary is indicated by red arrowhead and red broken lines. Snap shot images from Videos S4 and S5 showing the epidermal cell divisions. Division angles with respect to the A–P axis (0°–30°, 31°–60°, 61°–90°) are shown by white, yellow, and red lines, respectively. 0 min indicates the start of the observation. Scale bars, 20 μm.

(B and C) Angle of division orientation with respect to the A–P axis in DMSO-treated controls (B) and Ciliobrevin D-treated embryos (C). In the DMSO-treated controls (n = 5 embryos), the values were extracted from 14 cells for row A, 15 cells for row 1, 16 cells for row 2, 16 cells for row P, and 40 cells for row PP. Data are represented as individual values and boxplots. Means are indicated as red horizontal bars. Medians are indicated with dashed lines. Boxes indicate second and third quartiles, and whiskers indicate the maximum and minimum values. In the Ciliobrevin D-treated embryos (n = 7 embryos), the values were extracted from 20 cells for row A, 16 cells for row 1, 23 cells for row 2, 17 cells for row P, and 65 cells for row PP. Data are represented as individual values and boxplots. Means are indicated as red horizontal bars. Medians are indicated with dashed lines. Boxes indicate second and third quartiles, and whiskers indicate the maximum and minimum values. There is no statistically significant difference in the cell rows A and 1 between the DMSO-treated control and Ciliobrevin D-treated embryos; however, the angles of the cell rows 2, P, and PP of the Ciliobrevin D-treated embryos were significantly higher than those of the control embryos.

(D) Phenotype of Ciliobrevin D-treated embryos and quantitative evaluation of the epithelial bending. See Transparent Methods for the calculation methods. Table shows the results of calculations. N.S. and *** indicate p > 0.05 and p < 0.001, respectively (t test). Scale bar, 100 μm.

(E) The width of the trunk and tail regions and the tail length in the DMSO-treated control and Ciliobrevin D-treated embryos. See Transparent Methods for the calculation methods. N.S. and *** indicate p > 0.05 and p < 0.001, respectively (t test). Note that the trunk in the Ciliobrevin D-treated embryos is significantly wider than that in control embryos for unknown reason.

(F) Characterization of the morphogenetic change during the formation of epithelial bending. The width of the trunk and tail regions (ventral view) and the tail length before and after the epithelial bending formation. See Transparent Methods for the calculation methods. Table shows the results of calculations. N.S. and *** indicate p > 0.05 and p < 0.001, respectively (t test). Scale bar, 100 μm.

different calculation methods (Figure 4D). In addition, these embryos had wider and shorter tails than did normal embryos (Figure 4E) (214.7 μm for the Ciliobrevin D-treated tail width versus 180.6 μm for control, p < 0.001, t test; 180.8 μm for the Ciliobrevin D-treated tail length versus 237.7 μm for control, p < 0.001, t test). In the normal epithelial bending formation, the tail becomes relatively thinner when compared with the trunk and longer (Figure 4F). We also noticed that, in the Ciliobrevin D-treated embryos, cell divisions were delayed (Figure S2). However, this delay is not likely a cause of the phenotype described above, because treatment with the inhibitor under different conditions (at 10 μM for 2 h) further delayed cell division but did not affect the shaping of the tailbud embryo (Figure S2).

Along with Ciliobrevin D, we used another dynein inhibitor EHNA and observed its effect on the epithelial bending and tailbud shape formation. EHNA is reported to be less specific (Firestone et al., 2012), but it has been shown to disrupt mitotic spindle orientation in another ascidian species, *Ciona intestinalis* (Negishi and Yasuo, 2015). The EHNA treatment abrogated cell division orientation (Figures S3A and S3B; Video S6) in a manner similar to that with Ciliobrevin D treatment, with significantly less bending (Figure S3C) and wider and shorter tail (Figure S3D) when compared with control embryos; however, the morphologies of the resultant tailbud embryo seemed to differ between the two inhibitor treatments (Figures 4D and S3C). In fact, the EHNA-treated tail was significantly thinner and longer than the Ciliobrevin D-treated one (191.3 μm for the EHNA-treated tail width [Figure S3D] versus 214.7 μm for the Ciliobrevin D-treated tail width [Figure 4E], p < 0.001, t test; 215.0 μm for the EHNA-treated tail length [Figure S3D] versus 180.8 μm for the Ciliobrevin D-treated tail length [Figure 4E], p < 0.001, t test), possibly due to less inhibitory effect of EHNA on cell division orientation (a division angle of 42.2° on average with respect to the A–P axis for EHNA-treated cells of the row PP [Figure S3B] versus 53.3° for Ciliobrevin D-treated PP cells [Figure 4C] and/or to the non-specific effect of EHNA).

These results suggest that the mitotic spindle rotation is dynein dependent and required for the tailbud shaping.

Anterior Enrichment of Dynein Protein in Posterior Epidermal Cells

We then investigated whether dynein protein is enriched in a localized cell cortical domain of posterior epidermal cells, as is shown in several asymmetrically dividing cells undergoing mitotic spindle rotations (Lu and Johnston, 2013; di Pietro et al., 2016). To observe sub-cellular localization of dynein protein, we first performed antibody staining using anti-dynein heavy chain antibody, which has been used successfully to locate dynein protein in early embryonic cells of another ascidian species, *C. intestinalis* (Negishi and Yasuo, 2015). The antibody staining suggested that dynein protein is present at the cell cortex and the peri-nuclear region of posterior epidermal cells (Figure 5A). Significantly, signals for dynein at the cell cortex were more concentrated to the anterior edge of cells (Figure 5A). The average ratio of the anterior to the posterior dynein signal intensities was 1.51 (Figure 5B, n = 108, S.D. = 0.39). The anterior
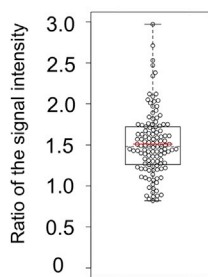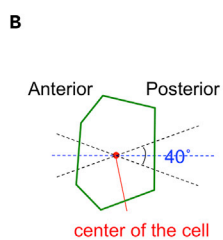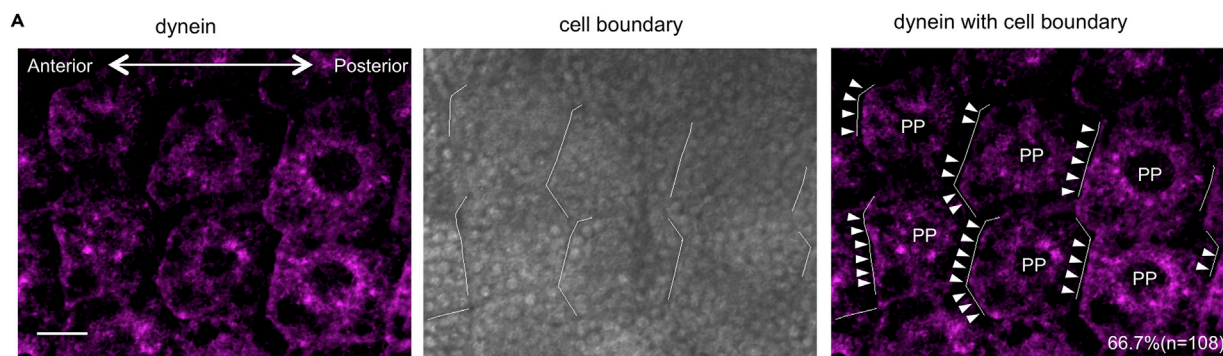
A

dynein

cell boundary

dynein with cell boundary

66.7%(n=108)

B

Relative signal intensity of the anterior
to the posterior surfaces of the cells

C

DCIC-EGFP

PH-dTomato

DCIC-EGFP and PH-dTomato

69.2 %(n=26)

C4
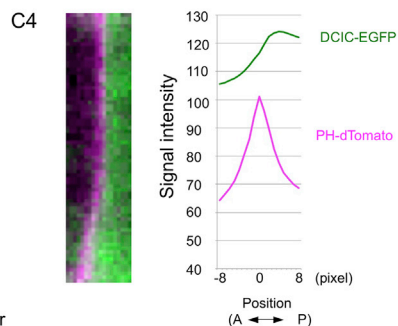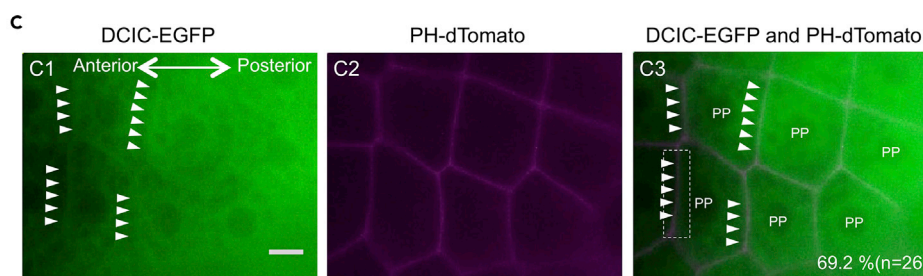
Average signal intensities of DCIC-
EGFP and PH-dTomato along the A–P
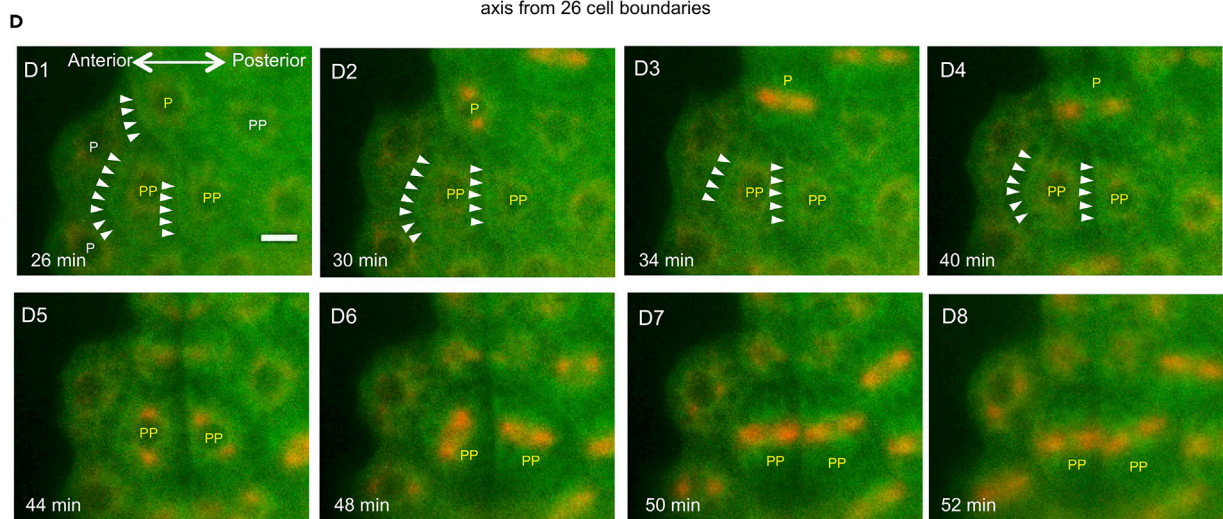axis from 26 cell boundaries

D

Figure 5. Enrichment of Dynein in the Anterior Surface of the Cells before the Spindle Rotation

(A) Images of anti-dynein antibody staining of the cells in the row PP are shown. Anterior is to the left. (Left) Dynein signal is observed at the cellular surface of the cells and around the nucleus. (Middle) Cell boundary (white line) is identified by separating cell-cell contact after squishing the specimen. (Right) A merged image of the left and middle images indicating the enriched cell cortex signal is from the anterior of the cells (arrowheads). Scale bar, 10 μm.

(B) Quantification of the dynein protein enrichment. (Top) Schematic diagram showing how to measure the signal intensity. (Bottom) Relative signal intensity of the anterior to the posterior surfaces of the cells. All the cells with cell boundaries identified by squishing were measured. See Transparent Methods for the calculation methods. Data are represented as individual values and boxplot. The mean is indicated as a red horizontal bar. The median is indicated with dashed line. Box indicates the second and third quartiles, and whiskers indicate the maximum and minimum values.

(C) Images of DCIC-EGFP and PH-dTomato fluorescent signals in the row PP cells. (C1) Dynein signal is observed in the surface of PP cells (arrowheads). Scale bar, 10 μm. (C2) PH-dTomato signal (magenta) is detected at the cell membrane of PP cells. (C3) A merged image of C1 and C2. (C4, left) A close-up view of the adjacent cell surfaces between PP cells (a dot-lined square in C3). Brightness and contrast were enhanced for visualization. (C4, right) Average signal intensities of DCIC-EGFP and PH-dTomato from 26 different cell surfaces. See Transparent Methods for the calculation method. Note that DCIC-EGFP signal was peaked posterior to the PH-dTomato peak, indicating that DCIC-EGFP signal is enriched in the anterior surface of the cell.

(D) Selected snapshot images from Video S7 showing the expression of DCIC-EGFP (for dynein, green) and MAP7-mCherry (for spindle orientation, red) in posterior epidermal cells. Anterior is to the left. P and PP represent cells in the rows P and PP, respectively. Cell boundaries between different rows are not straight perpendicular to the A–P axis due to different timing of cell divisions (also see Figure 3B). Enrichment of the dynein is observed in the anterior surface of the cells (arrowheads). Time after the start of observation is shown in the bottom left of each image. The yellow P and PP indicate the cells in which dynein is observed in the anterior surface before spindle rotation. Scale bar, 10 μm.

localization was also confirmed by fluorescent observation using a fusion protein of dynein cytoplasmic intermediate chain (DCIC) to EGFP and PH-dTomato (Figure 5C). Further confirmation of these findings was obtained by live-imaging analysis, wherein mRNAs encoding DCIC-EGFP and MAP7-mCherry were injected. EGFP signals accumulated at the cell cortex, presumably at the anterior cortex of the cell, given the earlier results, and in the peri-nuclear region (Figure 5D; Video S7). Notably, the EGFP signals at the cell cortex were evident (cells P and PP with arrowheads in Figure 5D; Video S7) before the mitotic spindle rotation occurs (cells P and PP with arrowheads in Figure 5D; Video S7). These results suggest that posterior epidermal cells are polarized along the A–P axis with dynein protein accumulating at the cells' anterior edges and that the protein drives mitotic spindle rotation prior to cell division. We detected fluorescent signals suggesting anteriorly concentrated dynein protein accumulation in cells in row PP from both the antibody staining (60.0% [n = 30], Figure S4) and the live-imaging analysis (59.1% [n = 22], Figure 5D and Video S7); however, the percentages were small for cells in rows 2 (18.2% [n = 11]) and P (7.7% [n = 13]) from the antibody staining. In most of the cells in rows 2 and P, the protein was present at the cell cortex and showed no obvious bias in its localization along the A–P axis (Figure S4).

Autonomous Cell Division Reorientation to the Epithelial Sheet

To obtain an insight into the mechanisms of cell division reorientation, we examined possible involvement of the underlying tissues such as muscle and notochord. We manually isolated the epidermal layer of the lateral side of the embryo from the underlying tissues approximately 40 min after neurula rotation (Nishide et al., 2012) (i.e., approximately 45 min before the cell divisions) and observed the patterns of division of epidermal cells in the isolated layer. We found that majority of the epidermal cells in rows 2, P, and PP in the isolated layer divided along the A–P axis, whereas the cells in rows A and 1 divided more in a circumferential direction (Figures 6A and 6B; Video S8), as observed in the intact embryos (Figure 2). Therefore, underlying tissues do not appear to affect the division reorientation of epidermal cells in the posterior region, at least after the 40-min mark after neurula rotation (45 min prior to the cell divisions). Notably, an initial step of convergent extension movement of the notochord occurred between 1 h 30 min and 2 h after neurula rotation (Figures 6C and 6D), eliminating the possibility that cell division orientation in the overlying epidermal cells is affected by physical force generated by the notochord extension along the A–P axis.

DISCUSSION

In this study, we found a mechanism by which epithelial bending and overall tailbud body shape is generated during animal development. The mechanism for shaping an ascidian tailbud embryo centers on cell divisions, with division orientations between two adjacent regions of the epithelial layer directed perpendicular to each other. The differently oriented cell divisions in the adjacent regions produce a relative narrowing in one region and the layer ends up with a bending at their boundary.
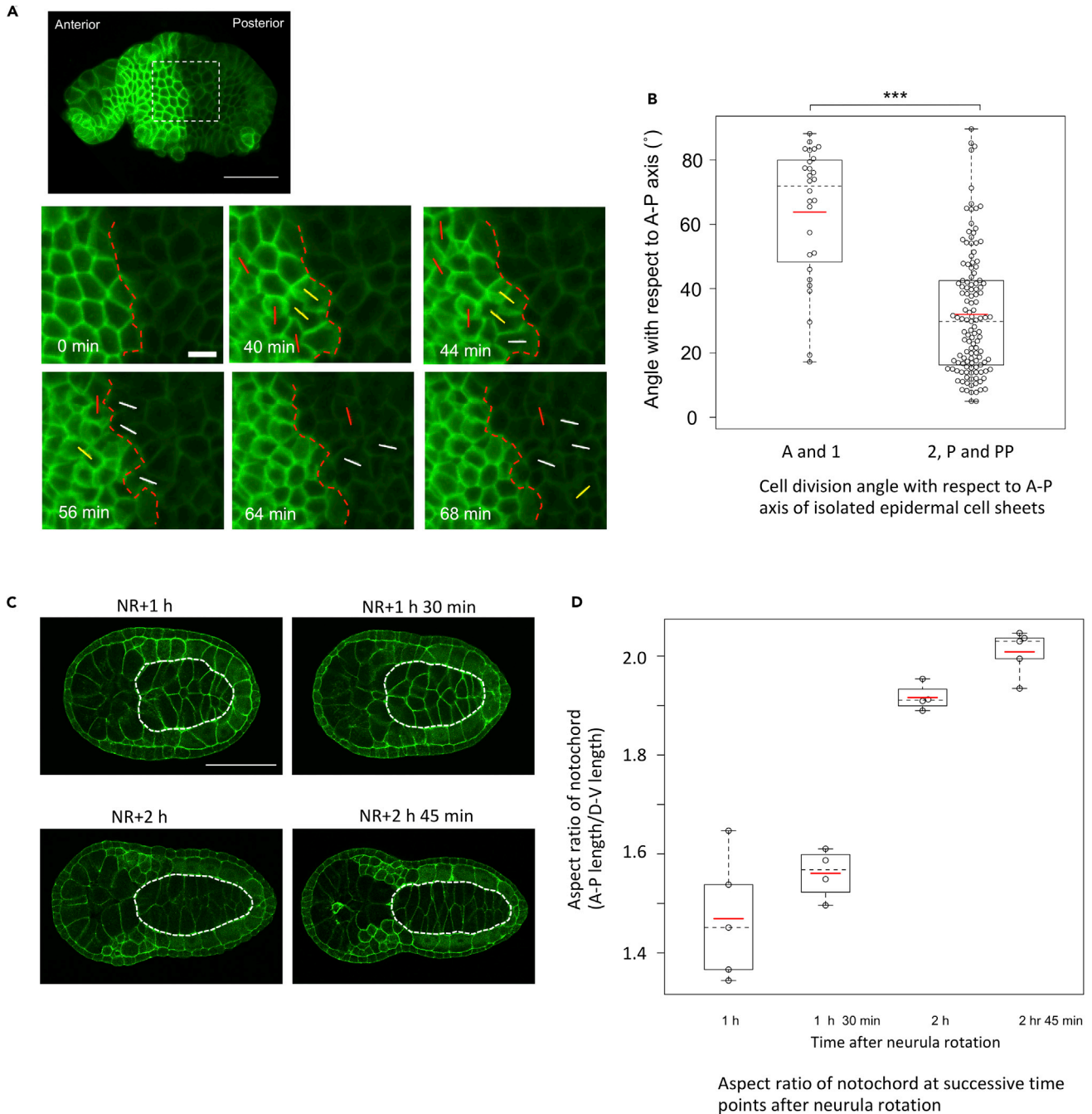
Figure 6. Cell Division Pattern in Isolated Epidermal Cell Sheets

(A and B) Division pattern of the isolated epidermal cells. (A) Snap shots images from Video S8 showing epidermal cell division in isolated epidermal cell sheet. Anterior is to the left. The lineage boundary is indicated in red broken lines. Division angles with respect to the A–P axis (0°–30°, 31°–60°, 61°–90°) are shown with white, yellow, and red lines, respectively. Time after the start of observation is shown in the left bottom of each image. Scale bar, 20 μm. (B) Division angle with respect to the A–P axis in the cell rows A, 1 and 2, P and PP. Each dot represents a single observed cell. In the cell rows A and 1 (n = 5 embryos), the values were extracted from 28 cells. In the cell rows 2, P and PP (n = 5 embryos), the values were extracted from 79 cells. Data are represented as individual values and boxplots. Means are indicated as red horizontal bars. Medians are indicated with dashed lines. Boxes indicate second and third quartiles, and whiskers indicate the maximum and minimum values. The difference of the division angle between these two groups was statistically significant. *** indicates p < 0.001 (t test).

Figure 6. *Continued*

(C and D) Characterization of notochord convergent extension. (C) Images of Phallacidin-stained embryos at different stages from the neurula to the early tailbud stages (NR+1 h, NR+1 h 30 min, NR+2 h, NR+2 h 45 min). At each stage, the frontal section is shown with the notochord outlined by white broken lines. Anterior is to the left. (D) Aspect ratio of the notochord at each stage. Each circle represents one embryo. Data are represented as individual values and boxplots. Means are indicated as red horizontal bars. Medians are indicated with dashed lines. Boxes indicate second and third quartiles, and whiskers indicate the maximum and minimum values. Aspect ratio is increased highly from the NR+1 h 30 min to the NR+2 h.

Possible Other Mechanisms for the Epithelial Bending Formation

Although our present findings suggest that an ascidian tailbud embryo is shaped by the two-directional epithelial layer transformation by different cell division orientations, we cannot rule out the involvement of other mechanisms.

Initially, we suspected that an anisotropic apical constriction of epidermal cells at the future bending region may have a role in the formation of epithelial bending. The rectangular shape of the cells in that region (Figure 1B2) was reminiscent of the mesoderm precursor cells undergoing anisotropic apical constriction in the ventral midline of gastrulating *Drosophila* embryos (Dawes-Hoang et al., 2005; Fox and Peifer, 2007; Sawyer et al., 2010). However, for the following reasons, we concluded that this is not the case. First, in the frontal section of the embryos, the epidermal cells at the bending region did not display a wedge-like shape along the apico-basal axis (Figures 1A3 and 1A4). Second, the deepest point of the epithelial bending did not coincide with the center point of the rectangular-shaped cell rows (in this case, the interface of rows 1 and 2) (Figures 1B2 and 1B3). Coincidence with the center point would have been observed if bending is driven by anisotropic apical constriction.

Another mechanism that may contribute to the formation of epithelial bending is a shortening of the lateral sides of the epidermal cells along the apico-basal axis. A shortening of cells drives invagination of endoderm cells during gastrulation in another ascidian species (Sherrard et al., 2010). We observed that epidermal cells around the future bending site were extended along the apico-basal axis longer than were other epidermal cells located more anteriorly and posteriorly prior to the formation of bending (Figure 1A2) but their length was reduced to that of the other cells upon formation of the epithelial bending (Figures 1A3 and 1A4). This could explain why there was still a small degree of bending in embryos treated with Ciliobrevin D (Figure 4D). Moreover, EHNA treatment reduced epithelial bending by a significantly greater extent than did Ciliobrevin D according to one of our calculation methods (8.18 μm in Figure 4D [Ciliobrevin D] versus 6.34 μm in Figure S3C [EHNA] calculated by Method 2, p < 0.001 [t test]) despite the fact that it still generated longer and thinner tails than did Ciliobrevin D (Figures 4 and S3). EHNA has been reported to be less specific to dynein inhibition and to interfere with actin-dependent cellular processes (Schliwa et al., 1984). Consequently, the EHNA treatment may have affected the shortening of the epidermal cells through inhibiting actin function and reducing the extent of the epithelial bending.

It may also be possible that tissues underlying the epidermal layer, such as muscle and notochord, are involved in the formation of epithelial bending and the tailbud shaping. Although our isolation experiment of the epidermal layer suggests that epidermal cells undergo division reorientation without the underlying tissue (Figure 6A), it is still possible that underlying tissues are involved in ways other than regulation of cell division orientation. Suggestively, the boundary between underlying tissues, namely, mesenchyme and muscle, appears to coincide with the epithelial bending position.

Environmental Factors Required for the Tailbud Shaping

Our model for shaping the ascidian tailbud embryo (Figure 3E) would be valid if the field around the embryo's circumference is resistant to a tension generated in the posterior region by the differently oriented cell divisions in the two adjacent regions (Figure S5A, top). Accordingly, the constriction in the posterior region would properly take place as a result of the cell divisions. We speculate that the neural tube closure (Hashimoto et al., 2015; Ogura and Sasakura, 2016) could provide such a field, as we had found that the neural tube was nearly closed (two-thirds to three-quarters from the posterior end) when the epidermal cells divided (100% [n = 46]). If the neural tube is not closed, it is likely that the tension generated by the differently oriented cell division would not be propagated normally around the circumference of the embryo and posterior region would not be constricted (Figure S5A, bottom). Although our current approaches (see the Limitations of the Study section) are inconclusive, it is tempting to propose the importance of "a chain of morphogenetic events" for the correct shaping of individual tissues in the scale of the whole

organism, in which one event (in this case, neural tube closure) influences another event (tailbud shaping) occurring at a different place and time. Recently, it has been reported that neural tube closure is necessary for correct orientation of cell division and epidermal stratification in mouse embryos (Box et al., 2019). Consequently, future studies will be required to examine whether the interactive regulation of spatially and temporally different morphogenetic events is a common characteristic in animal morphogenesis.

Determination of the Position of the Division Orientation Boundary

Our present findings suggest that determination of the position of the epithelial bending along the A–P axis in the neurula embryo relies on the position of the cell division orientation boundary. We speculate that the position of the division orientation boundary along the A–P axis is determined by the cell lineage, rather than by extracellular signals occurring at a later stage—such as antagonistic signals for patterning the neurula embryo along the A–P axis (Pasini et al., 2012)—because the division orientation boundary fell consistently at the same position with respect to the A–P lineage boundary in the ectoderm (i.e., one cell row away anteriorly) in different individuals (Figures 2B and 2C). As early as the second cell cleavage after fertilization that separates the A–P lineage, a difference could be made between the two lineages and memorized until it comes into effect at the late neurula stage. One candidate for the identity of the difference could be a member(s) of *Postplasmic/Pem* RNAs, a group of maternal mRNAs that are localized to the future posterior region of the egg and are inherited by posterior cells during cleavage stages (Makabe and Nishida, 2012; Sardet et al., 2005; Prodon et al., 2007). Although previous studies on *Postplasmic/Pem* RNAs have identified their function in determination of developmental fate (Nishida and Sawada, 2001; Nakamura et al., 2006) and regulation of cell division patterning (Negishi et al., 2007; Prodon et al., 2010) in the posterior-vegetal cells (mesoderm and endoderm), one member named Pem has been shown to repress anterior ectodermal genes, such as FoxA and SoxB1, in posterior-animal cells (ectoderm) at the eight-cell stage (Kumano et al., 2011).

Currently, it is also unclear as to how the division orientation boundary is placed one cell row anterior to the A–P lineage boundary. We determined that posterior epidermal cells are polarized along the A–P axis, and, therefore, planar cell polarity (PCP) pathway may contribute to establishing cell polarization. PCP is known to be propagated in the *Drosophila* wing disc, from the prospective proximal region to the prospective distal region, to pattern the orientation of wing hair (Ambegaonkar et al., 2012; Devenport, 2014). In the ascidian *Ciona savignyi*, a polarizing signal has been shown to be propagated from a notochord cell to establish PCP in an adjacent notochord cell located anteriorly (Kourakis et al., 2014). Based on these findings, we speculate that, in the *H. roretzi* neurula embryo, the epidermal cells in row 2, the only cells that undergo spindle rotations derived from the anterior ectoderm lineage, may receive a polarizing signal from the cells derived from the posterior ectoderm lineage. However, we observed that the majority of the epidermal cells in row PP are polarized in terms of localization of dynein protein (Figures 5 and S4; Video S7), whereas those in rows 2 and P are not (Figure S4). Therefore, the cells that share the boundary of the A–P lineages, both those in row 2 that share it posteriorly and those in row P that share it anteriorly, may behave differently owing to their contact with the different lineage cells across the boundary. However, they still undergo rotation of the mitotic spindle in a dynein-dependent manner (Figures 4A, 4B, S3A, and S3B; Videos S5 and S6).

Shaping of the Tailbud Embryo in Another Ascidian Species

The shape of the tailbud embryo is conserved in different ascidian species, with epithelial bending formed in the middle of the embryo along the A–P axis and the tail region becoming thinner and longer (Hotta et al., 2007). However, study has shown that most of the epidermal cells in both the anterior and posterior regions of the neurula embryo in the ascidian *C. intestinalis* type A (Currently *C. robusta*) divide along the A–P axis at their 11th divisions (Ogura et al., 2011; Negishi et al., 2016). In addition, live-imaging observation indicated that the timing of an epithelial bending to shape the tailbud embryo of *Ciona* seemed not to coincide with the 11th cell divisions (Negishi et al., 2016; Negishi, personal communication). Therefore, *H. roretzi* and *C. intestinalis* type A (Currently *C. robusta*) may use different mechanisms for shaping the tailbud embryo and may exemplify a phenomenon known as developmental system drift, whereby divergence of underlying molecular mechanisms occurs for conserved tissue development across species (Lemaire and Piette, 2015; True and Haag, 2001).

Limitations of the Study

As discussed above, the relationship between neural tube closure and tailbud shaping is still speculative. At present we have tried to address this issue by the following approaches.

We prevented the neural tube from closing by removing the chorion, as has been reported (Nishida and Satoh, 1985), at the late gastrula stage, and determined, via the four calculation methods described earlier, that such embryos failed to shape the normal tailbud embryos with a reduced extent of epithelial bending and wider and shorter tail (Figures S5B and S5C). However, these embryos exhibited the normal pattern of cell division—around the circumference of the embryo in the anterior versus along the A–P axis in the posterior regions (Figures S5D and S5E; Video S9)—suggesting that the failure is not due to an abrogated pattern of cell division.

We also tried to make the field around the embryo's circumference less resistant to a tension generated by cell division by culturing embryos in Ca^{2+}-free sea water, thereby weakening cell-cell adhesion. From right after the neural tube had been closed to two-thirds but before cell division, embryos were cultured in the absence of Ca^{2+}. These embryos exhibited a reduced extent of epithelial bending and wider and shorter tail (Figures S6A and S6B) but normal cell division orientations (Figures S6C and S6D).

These results support our speculation that a resistant field to the tension around the circumference of the embryo created by the neural tube closure could be necessary for shaping the epithelial bending and the tailbud embryo. However, non-specific effects cannot be ruled out in these experiments.

In another ascidian *C. intestinalis* type A (currently *C. robusta*), neural tube closure was successfully blocked by targeted overexpression of a dominant-negative form of RhoA (Hashimoto et al., 2015) and Cadherin 2 (Hashimoto and Munro, 2019) to dorsal midline cells including neural and epidermal cells flanking the boundary of the both cell types. Therefore, for the future prospective, it would be worthwhile to evaluate the epithelial bending and tailbud shape formation in *H. roretzi* embryos upon such more specific treatments to disrupt neural tube closure. These studies would shed light on an interactive regulation of spatially and temporally different morphogenetic events and its importance for tissue morphogenesis.

METHODS

All methods can be found in the accompanying Transparent Methods supplemental file.

SUPPLEMENTAL INFORMATION

Supplemental Information can be found online at https://doi.org/10.1016/j.isci.2020.100964.

ACKNOWLEDGMENTS

AUTHOR CONTRIBUTIONS

G.K. provided supervision and conceptualization. A.N. and G.K. designed experiments. A.N. conducted most of the experiments and analyzed the results. A.N. wrote the manuscript, and A.N. and G. K. revised it. A.N. and G.K. secured the funding.

DECLARATION OF INTERESTS

The authors declare no competing interests.

REFERENCES

Ambegaonkar, A.A., Pan, G., Mani, M., Feng, Y., and Irvine, K.D. (2012). Propagation of Dachsous-Fat planar cell polarity. Curr. Biol. *22*, 1302–1308.

Ambrosini, A., Rayer, M., Monier, B., and Suzanne, M. (2019). Mechanical function of the nucleus in force generation during epithelial morphogenesis. Dev. Cell *50*, 1–15.

Bergstralh, D.T., Dawney, N.S., and St Johnston, D. (2017). Spindle orientation: a question of complex positioning. Development *144*, 1137–1145.

Bowman, S.K., Neumüller, R.A., Novatchkova, M., Du, Q., and Knoblich, J.A. (2006). The Drosophila NuMA Homolog Mud regulates spindle orientation in asymmetric cell division. Dev. Cell *10*, 731–742.

Box, K., Joyce, B.W., and Devenport, D. (2019). Epithelial geometry regulates spindle orientation and progenitor fate during formation of the mammalian epidermis. Elife *8*, https://doi.org/10.7554/eLife.47102.

Brun-Usan, M., Marín-Riera, M., Grande, C., Truchado-Garcia, M., and Salazar-Ciudad, I. (2017). A set of simple cell processes is sufficient to model spiral cleavage. Development *144*, 54–62.

Colombo, K., Grill, S.W., Kimple, R.J., Willard, F.S., Siderovski, D.P., and Gönczy, P. (2003). Translation of polarity cues into asymmetric spindle positioning in *Caenorhabditis elegans* embryos. Science *300*, 1957–1961.

Conklin, E.G. (1905). The organization and cell lineage of the ascidian egg. J. Acad. Nat. Sci. (Phila.) *13*, 1–119.

da Silva, S.M., and Vincent, J.P. (2007). Oriented cell divisions in the extending germband of Drosophila. Development *134*, 3049–3054.

Davidson, L.A. (2012). Epithelial machines that shape the embryo. Trends Cell Biol. *22*, 82–87.

Dawes-Hoang, R.E., Parmar, K.M., Christiansen, A.E., Phelps, C.B., Brand, A.H., and Wieschaus, E.F. (2005). Folded gastrulation, cell shape change and the control of myosin localization. Development *132*, 4165–4178.

Devenport, D. (2014). The cell biology of planar cell polarity. J. Cell Biol. *207*, 171–179.

di Pietro, F., Echard, A., and Morin, X. (2016). Regulation of mitotic spindle orientation: an integrated view. EMBO Rep. *17*, 1106–1130.

Du, Q., and Macara, I.G. (2004). Mammalian Pins is a conformational switch that links NuMA to heterotrimeric G proteins. Cell *119*, 503–516.

Firestone, A.J., Weinger, J.S., Maldonado, M., Barlan, K., Langston, L.D., O'Donnell, M., Gelfand, V.I., Kapoor, T.M., and Chen, J.K. (2012). Small-molecule inhibitors of the AAA+ ATPase motor cytoplasmic dynein. Nature *484*, 125–129.

Fox, D.T., and Peifer, M. (2007). Abelson kinase (Abl) and RhoGEF2 regulate actin organization during cell constriction in Drosophila. Development *134*, 567–578.

Grill, S.W., and Hyman, A.A. (2005). Spindle positioning by cortical pulling forces. Dev. Cell *8*, 461–465.

Guerrier, P. (1970). Les caracteres de la segmentation et la determination de la polarite dorsoventrale dans le developpement de quelques Spiralia I. Les formes a premier clivage egal. J. Embryol. Exp. Morphol. *23*, 611–637.

Hashimoto, H., Robin, F.B., Sherrard, K.M., and Munro, E.M. (2015). Sequential contraction and exchange of apical junctions drives zippering and neural tube closure in a simple chordate. Dev. Cell *32*, 241–255.

Hashimoto, H., and Munro, E. (2019). Differential expression of a classic Cadherin directs tissue-level contractile asymmetry during neural tube closure. Dev. Cell *51*, 158–172.

Hertwig, O. (1884). Das Problem der Befruchtung und der Isotropie des Eies. Eine Theorie der Vererbung. Jen. Z. Med. Naturwiss. *18*, 276–318.

Hotta, K., Mitsuhara, K., Takahashi, H., Inaba, K., Oka, K., Gojobori, T., and Ikeo, K. (2007). A web-based interactive developmental table for the ascidian *Ciona intestinalis*, including 3D real-image embryo reconstructions: I. From fertilized egg to hatching larva. Dev. Dyn. *236*, 1790–1805.

Kondo, T., and Hayashi, S. (2013). Mitotic cell rounding accelerates epithelial invagination. Nature *494*, 125–129.

Kourakis, M.J., Reeves, W., Newman-Smith, E., Maury, B., Abdul-Wajid, S., and Smith, W.C. (2014). A one-dimensional model of PCP signaling: polarized cell behavior in the notochord of the ascidian Ciona. Dev. Biol. *395*, 120–130.

Kumano, G., and Nishida, H. (2007). Ascidian embryonic development: an emerging model system for the study of cell fate specification in chordates. Dev. Dyn. *236*, 1732–1747.

Kumano, G., Takatori, N., Negishi, T., Takada, T., and Nishida, H. (2011). A maternal factor unique to ascidians silences the germline via binding to P-TEFb and RNAP II regulation. Curr. Biol. *21*, 1308–1313.

Kuwajima, M., Kumano, G., and Nishida, H. (2014). Regulation of the number of cell division rounds by tissue-specific transcription factors and Cdk inhibitor during ascidian embryogenesis. PLoS One *9*, e90188.

Lechler, T., and Fuchs, E. (2005). Asymmetric cell divisions promote stratification and differentiation of mammalian skin. Nature *437*, 275–280.

Lecland, N., and Lüders, J. (2014). The dynamics of microtubule minus ends in the human mitotic spindle. Nat. Cell Biol. *16*, 770–778.

Lemaire, P., and Piette, J. (2015). Tunicates: exploring the sea shores and roaming the open ocean. A tribute to Thomas Huxley. Open Biol. *5*, 150053.

Lu, M.S., and Johnston, C.A. (2013). Molecular pathways regulating mitotic spindle orientation in animal cells. Development *140*, 1843–1856.

Makabe, K.W., and Nishida, H. (2012). Cytoplasmic localization and reorganization in ascidian eggs: role of postplasmic/PEMRNAs in axis formation and fate determination. Wiley Interdiscip. Rev. Dev. Biol. *1*, 501–518.

Martin, A.C., and Goldstein, B. (2014). Apical constriction: themes and variations on a cellular mechanism driving morphogenesis. Development *141*, 1987–1998.

McDougall, A., Chenevert, J., Prulière, G., Costache, V., Hébras, C., Salez, G., and Dumollard, R. (2015). Centrosomes and spindles in ascidian embryos and eggs. Methods Cell Biol. *129*, 317–339.

McGrew, M.J., Sherman, A., Lillico, S.G., Ellard, F.M., Radcliffe, P.A., Gilhooley, H.J., Mitrophanous, K.A., Cambray, N., Wilson, V., and Sang, H. (2008). Localised axial progenitor cell populations in the avian tail bud are not committed to a posterior Hox identity. Development *135*, 2289–2299.

Meshcheryakov, V.N., and Beloussov, L.V. (1975). Asymmetrical rotations of blastomeres in early cleavage of gastropoda. Wilhelm Roux Arch. Dev. Biol. *177*, 193–203.

Minc, N., Burgess, D., and Chang, F. (2011). Influence of cell geometry on division-plane positioning. Cell *144*, 414–426.

Minc, N., and Piel, M. (2012). Predicting division plane position and orientation. Trends Cell Biol. *22*, 193–200.

Morin, X., and Bellaïche, Y. (2011). Mitotic spindle orientation in asymmetric and symmetric cell divisions during animal development. Dev. Cell *21*, 102–119.

Munro, E.M., and Odell, G. (2002a). Morphogenetic pattern formation during ascidian notochord formation is regulative and highly robust. Development *129*, 1–12.

Munro, E.M., and Odell, G.M. (2002b). Polarized basolateral cell motility underlies invagination and convergent extension of the ascidian notochord. Development *129*, 13–24.

Nakamura, Y., Makabe, K.W., and Nishida, H. (2006). The functional analysis of Type I postplasmic/PEM mRNAs in embryos of the ascidian *Halocynthia roretzi*. Dev. Genes Evol. *216*, 69–80.

Negishi, T., and Yasuo, H. (2015). Distinct modes of mitotic spindle orientation align cells in the dorsal midline of ascidian embryos. Dev. Biol. *408*, 66–78.

Negishi, T., Takada, T., Kawai, N., and Nishida, H. (2007). Localized PEM mRNA and protein are involved in cleavage-plane orientation and unequal cell divisions in ascidians. Curr. Biol. *17*, 1014–1025.

Negishi, T., Miyazaki, N., Murata, K., Yasuo, H., and Ueno, N. (2016). Physical association between a novel plasma-membrane structure and centrosome orients cell division. Elife *5*, https://doi.org/10.7554/eLife.16550.

Nishida, H., and Satoh, N. (1985). Cell lineage analysis in ascidian embryos by intracellular injection of a tracer enzyme. II. The 16- and 32-cell stages. Dev. Biol. *110*, 440–454.

Nishida, H., and Sawada, K. (2001). macho-1 encodes a localized mRNA in ascidian eggs that specifies muscle fate during embryogenesis. Nature *409*, 724–729.

Nishida, H. (1986). Cell division pattern during gastrulation of the ascidian, *Halocynthia roretzi*. Dev. Growth Differ. *28*, 191–201.

Nishida, H. (1987). Cell lineage analysis in ascidian embryos by intracellular injection of a tracer enzyme. III. Up to the tissue restricted stage. Dev. Biol. *121*, 526–541.

Nishide, K., Mugitani, M., Kumano, G., and Nishida, H. (2012). Neurula rotation determines left-right asymmetry in ascidian tadpole larvae. Development *139*, 1467–1475.

Ogura, Y., and Sasakura, Y. (2013). Ascidians as excellent models for studying cellular events in the chordate body plan. Biol. Bull. *224*, 227–236.

Ogura, Y., and Sasakura, Y. (2016). Developmental control of cell-cycle compensation provides a switch for patterned mitosis at the onset of chordate neurulation. Dev. Cell *37*, 148–161.

Ogura, Y., Sakaue-Sawano, A., Nakagawa, M., Satoh, N., Miyawaki, A., and Sasakura, Y. (2011). Coordination of mitosis and morphogenesis: role of a prolonged G2 phase during chordate neurulation. Development *138*, 577–587.

Panousopoulou, E., and Green, J.B.A. (2014). Spindle orientation processes in epithelial growth and organisation. Semin. Cell Dev. Biol. *34*, 124–132.

Pasini, A., Manenti, R., Rothbächer, U., and Lemaire, P. (2012). Antagonizing retinoic acid and FGF/MAPK pathways control posterior body patterning in the invertebrate chordate *Ciona intestinalis*. PLoS One *7*, e46193.

Passamaneck, Y.J., Hadjantonakis, A.-K., and Di Gregorio, A. (2007). Dynamic and polarized muscle cell behaviors accompany tail morphogenesis in the ascidian *Ciona intestinalis*. PLoS One *2*, e714.

Peyre, E., Jaouen, F., Saadaoui, M., Haren, L., Merdes, A., Durbec, P., and Morin, X. (2011). A lateral belt of cortical LGN and NuMA guides mitotic spindle movements and planar division in neuroepithelial cells. J. Cell Biol. *193*, 141–154.

Prodon, F., Yamada, L., Shirae-Kurabayashi, M., Nakamura, Y., and Sasakura, Y. (2007). Postplasmic/PEM RNAs: a class of localized maternal mRNAs with multiple roles in cell polarity and development in ascidian embryos. Dev. Dyn. *236*, 1698–1715.

Prodon, F., Chenevert, J., Hébras, C., Dumollard, R., Faure, E., Gonzalez-Garcia, J., Nishida, H., Sardet, C., and McDougall, A. (2010). Dual mechanism controls asymmetric spindle position in ascidian germ cell precursors. Development *137*, 2011–2021.

Rose, L., and Gönczy, P. (2014). Polarity establishment, asymmetric division and segregation of fate determinants in early *C. elegans* embryos. WormBook, 1–43, https://doi.org/10.1895/wormbook.1.30.2.

Saches, J. (1878). Uber die Anordnung der Zellen in jungsten Pflanzentheilen, *2* (Arbeiten des Botanisches Institut), pp. 46–104.

Sardet, C., Dru, P., and Prodon, F. (2005). Maternal determinants and mRNAs in the cortex of ascidian oocytes, zygotes and embryos. Biol. Cell *97*, 35–49.

Sawyer, J.M., Harrell, J.R., Shemer, G., Sullivan-Brown, J., Roh-Johnson, M., and Goldstein, B. (2010). Apical constriction: a cell shape change that can drive morphogenesis. Dev. Biol. *341*, 5–19.

Schaefer, M., Shevchenko, A., and Knoblich, J.A. (2000). A protein complex containing Inscuteable and the Galpha-binding protein Pins orients asymmetric cell divisions in Drosophila. Curr. Biol. *10*, 353–362.

Schliwa, M., Ezzell, R.M., and Euteneuer, U. (1984). erythro-9-[3-(2-Hydroxynonyl)]adenine is an effective inhibitor of cell motility and actin assembly. Proc. Natl. Acad. Sci. U S A *81*, 6044–6048.

Sherrard, K., Robin, F., Lemaire, P., and Munro, E. (2010). Sequential activation of apical and basolateral contractility drives ascidian endoderm invagination. Curr. Biol. *20*, 1499–1510.

Srinivasan, D.G., Fisk, R.M., Xu, H., and van den Heuvel, S. (2003). A complex of LIN-5 and GPR proteins regulates G protein signaling and spindle function in *C. elegans*. Genes Dev. *17*, 1225–1239.

Tall, E.G., Spector, I., Pentyala, S.N., Bitter, I., and Rebecchi, M.J. (2000). Dynamics of phosphatidylinositol 4,5-bisphosphate in actin-rich structures. Curr. Biol. *10*, 743–746.

True, J.R., and Haag, E.S. (2001). Developmental system drift and flexibility in evolutionary trajectories. Evol. Dev. *3*, 109–119.

Wang, Y.-C., Khan, Z., Kaschube, M., and Wieschaus, E.F. (2012). Differential positioning of adherens junctions is associated with initiation of epithelial folding. Nature *484*, 390–395.

Williams, T.A., and Nagy, L.M. (2017). Linking gene regulation to cell behaviors in the posterior growth zone of sequentially segmenting arthropods. Arthropod Struct. Dev. *46*, 380–394.

Supplemental Information

Dynein-Mediated Regional Cell Division

Reorientation Shapes a Tailbud Embryo
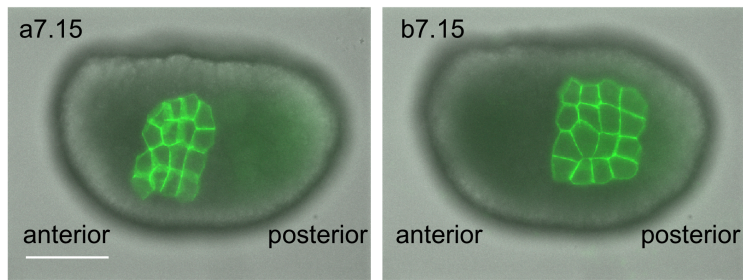
Ayaki Nakamoto and Gaku Kumano

Figure S1 (related to Figure 1)
The 11th epidermal cell division. Lateral side view, with anterior to the left. Scale bar, 100 µm. Either trunk epidermal precursor cell (a7.15) or tail epidermal precursor cell (b7.15) was injected with PH-YFP mRNA at the 64-cell stage (i.e., after the 6th division stage), and the number of descendants before the formation of epithelial bending was calculated. Both labeled cells divided to produce 16 cells (i.e. four times), indicating that the 10th division had been completed. Thus, the division during the formation of epithelial bending is the 11th. Also, the resulting squares of 4 × 4 cells may suggest that a7.15 and b7.15 underwent 4 rounds of alternate cell divisions at right angles to each other, highlighting a specific cell cycle undergoing division reorientation at the 11th division.
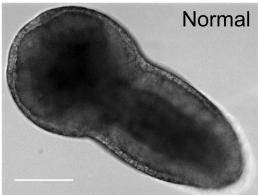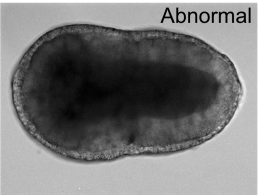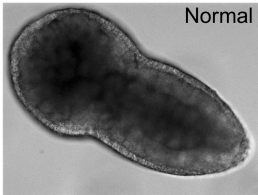
	Control 0.4% DMSO for 1 h (n=12)	30 µM Ciliobrevin D for 1 h (n=15)	10 µM Ciliobrevin D for 2 h (n=19)
Start of division (average ± s.d.)	NR+1 h 27 min ± 8 min	NR+2 h 57 min ± 4 min	NR+3 h 24 min ± 12 min
End of division (average ± s.d.)	NR+3 h 6 min ± 15 min	NR+5 h 3 min ± 7 min	NR+5 h 25 min ± 7 min
Period of the division	1 h 39 min	2 h 06 min	2 h 1 min
Epithelial bending	Normal	Abnormal	Normal

Figure S2 (related to Figure 1)
Effect of dynein inhibitor on cell division timing. Table showing the start of the cell division (top), the end of the cell division (middle), and the period of the cell division (bottom). The period of the division was calculated by subtracting the average of the start of division from the average of the end of the division. Scale bar, 100 µm. The definition of the start and the end of cell division is described in the methods section. Resultant tailbud embryos are shown under the table.

A

Angle with respect to A-P axis (°)

80
60
40
20
0

A 1 2 P PP

Division angle of each cell row in the embryos
treated with 0.4% DMSO (n=5 embryos)

B

N.S.
N.S.
***
***
***

Angle with respect to A-P axis (°)

80
60
40
20
0

A 1 2 P PP

Division angle of each cell row in the embryos
treated with 2 mM EHNA (n=5 embryos)

C

2 mM EHNA

Method 1

X Y

Method 2

Method 1	Y/X
Control (n=10)	0.77 (s.d. =0.036)
EHNA (n=11)	0.89 (s.d.=0.032)

***

Method 2	Depth of bending
Control (n=10)	16.69 µm (s.d. =3.37)
EHNA (n=11)	6.34 µm (s.d.=2.28)

***

D

Control

Trunk width (n=10)	214.4 µm (s.d. =8.73)
Tail width (n=10)	180.6 µm (s.d.=7.47)
Tail length (n=10)	237.7 µm (s.d.=10.45)

***

N.S.

EHNA treatment

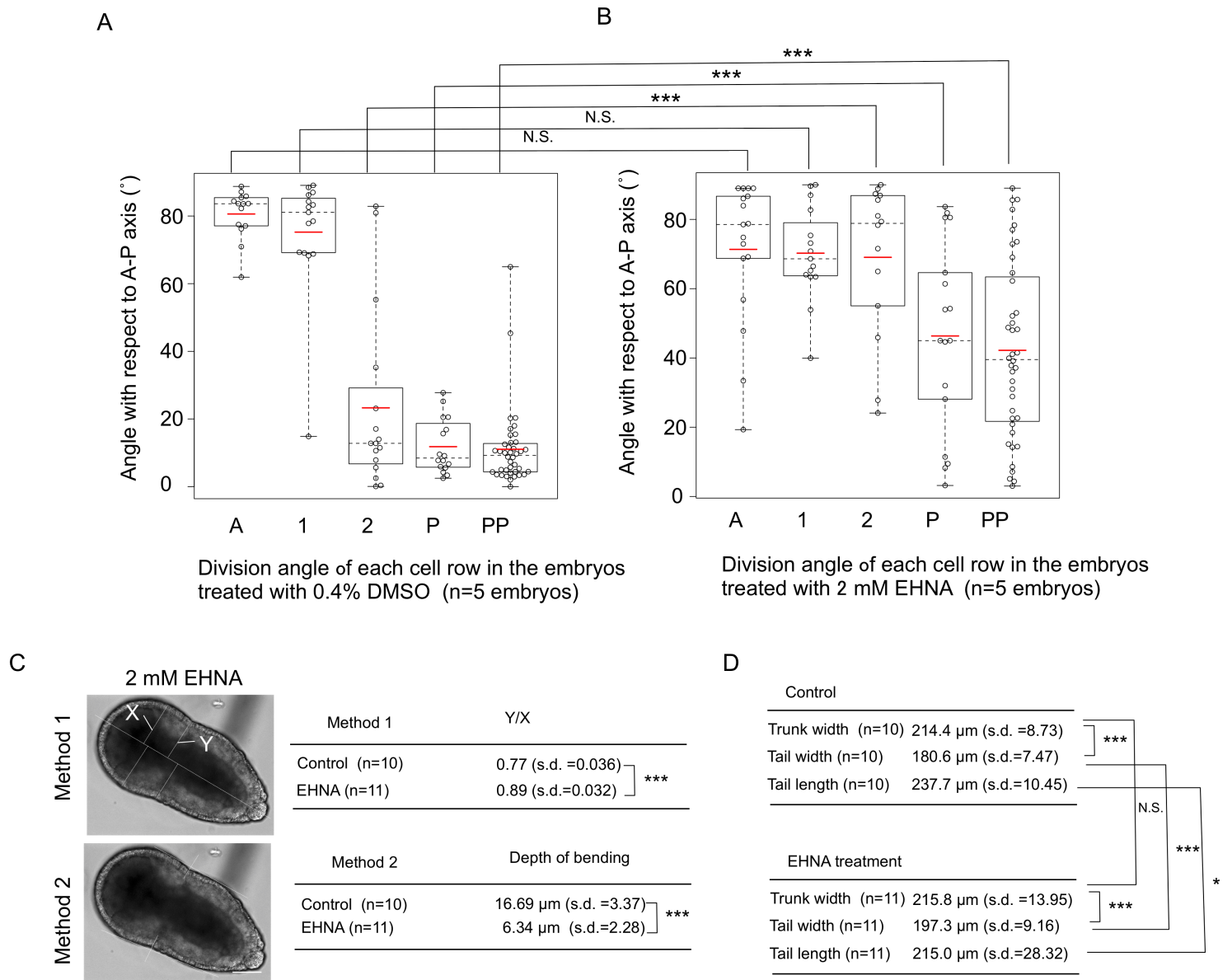| Trunk width (n=11)	215.8 µm (s.d. =13.95)
Tail width (n=11)	197.3 µm (s.d.=9.16)
Tail length (n=11)	215.0 µm (s.d.=28.32)

***
*
***

Figure S3 (related to Figure 4)
**Effect of dynein inhibitor EHNA on pattern of epidermal cell division and formation of epithelial
bending.** (A, B) Angle of division orientation with respect to the A–P axis in the DMSO-treated
control (A) and EHNA-treated embryos (B). The DMSO-treated embryos (n=5, Fig. 4B) were used as
the control. In the EHNA-treated embryos (n=5 embryos), the values were extracted from 17 cells for
row A, 15 cells for row 1, 14 cells for row 2, 17 cells for row P and 40 cells for row PP. Data are
represented as individual values and boxplots. Means are indicated as red horizontal bars. Medians are
indicated with dashed lines. Boxes indicate second and third quartiles, and whiskers indicate the
maximum and minimum values. There was no statistically significant difference in the cell rows A and
1 between the DMSO-treated control and EHNA-treated embryos; however, the angles of the cell rows
2, P and PP of the EHNA-treated embryos were significantly higher than those of the control embryos.
N.S. and *** indicate $p > 0.05$ and $p < 0.001$, respectively (T-test). (C) Phenotype of EHNA-treated
embryo and quantitative evaluation of the epithelial bending. See experimental procedure for the
calculation methods. Table shows the results of calculations. *** indicates $p < 0.001$ (T-test). Scale bars,
100 µm. (D) The width of the trunk and tail regions and the tail length in the DMSO-treated control
and EHNA-treated embryos. See experimental procedure for the calculation methods. N.S., * and ***
indicate $p > 0.05$, $p < 0.05$ and $p < 0.001$, respectively (T-test).
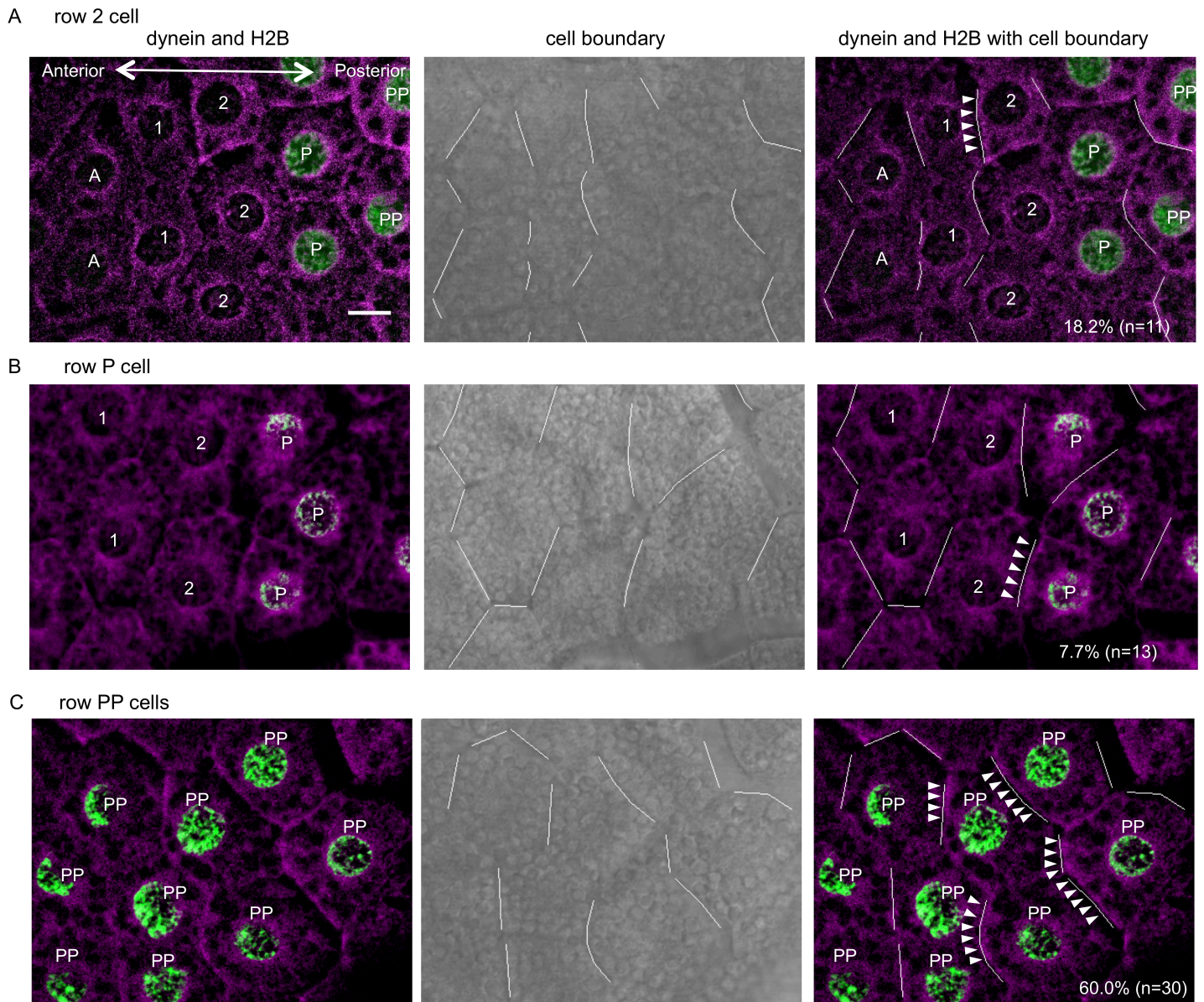
Figure S4 (related to Figure 5)
Dynein protein in localization in each cell row. Image of double staining for anti-dynein and anti-GFP antibody staining (A–C). Anti-GFP antibody recognizes the nuclei of the posterior epidermal cells, which are marked by H2B-GFP. H2B-GFP mRNA has been injected into a progenitor cell of the posterior epidermal cells at the 8-cell stage embryo (b4.2). Stained embryos were squished gently to separate cell–cell contact and to identify the cell boundary (middle), which is shown by a white line. The dynein signal was indicated by arrowheads when detected in the anterior side of the cells. A, 1, 2, P and PP represent cells in row A, 1, 2, P and PP, respectively, according to the GFP expression. The digits in the bottom right in the right-hand images show the proportion of the cells in which anterior localization was observed out of the cells whose cell boundaries were identified. Scale bar, 10 μm.
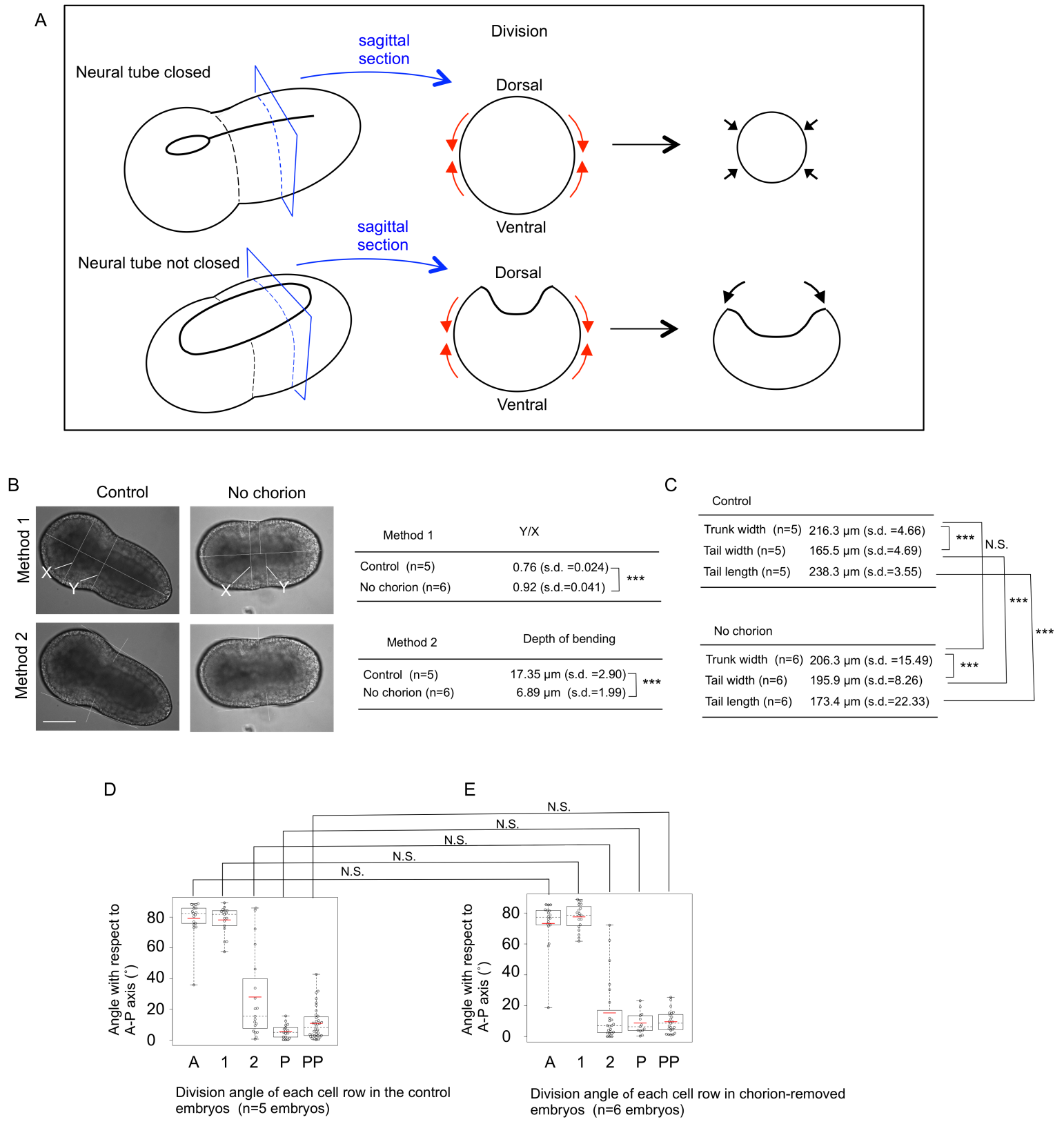
Figure S5 (related to Figure 6)
Effects of the chorion removal on the pattern of epidermal cell division and the formation of epithelial bending. (A) Schematic diagrams of predicted outcomes of epithelial cell divisions along the A–P axis on the thickness of the future tail region and thus the epithelial bending formation in embryos with (top) or without (bottom) the neural tube closure. Overall embryos are shown on the left with positions of sagittal sections shown on the right. Shown on the right are representatives of what might happen in the future tail region along the entire length of the region where epithelial cells divide along the A–P axis. Red arrows indicate predicted constricting forces generated around the

circumference of the embryos by the A–P oriented cell divisions. The force would not be propagated enough to constrict the circumference if it is not tied together throughout by the failure of the neural tube closure (black arrows, bottom-right). (B) Phenotype of chorion-removed embryo and quantitative evaluation of the epithelial bending. See experimental procedure for the calculation methods. Table shows the results of calculations. *** indicates p<0.001 (T-test). Scale bars, 100 μm. (C) The width of the trunk and tail regions and the tail length in the control and chorion-removed embryos. See experimental procedure for the calculation methods. N.S. and *** indicate p>0.05 and p<0.001, respectively (T-test). (D, E) Angle of division orientation with respect to the A–P axis in the intact control (D) and chorion-removed embryos (E). In the intact control (n=5 embryos), the values were extracted from 17 cells for row A, 17 cells for row 1, 19 cells for row 2, 17 cells for row P and 36 cells for row PP. In the chorion-removed embryos (n=6 embryos), the values were extracted from 18 cells for row A, 19 cells for row 1, 23 cells for row 2, 13 cells for row P and 23 cells for row PP. Data are represented as individual values and boxplots. Means are indicated as red horizontal bars. Medians are indicated with dashed lines. Boxes indicate second and third quartiles, and whiskers indicate the maximum and minimum values. There is no statistically significant difference between the intact control and chorion-removed embryos. N.S. indicates p>0.05 (T-test).
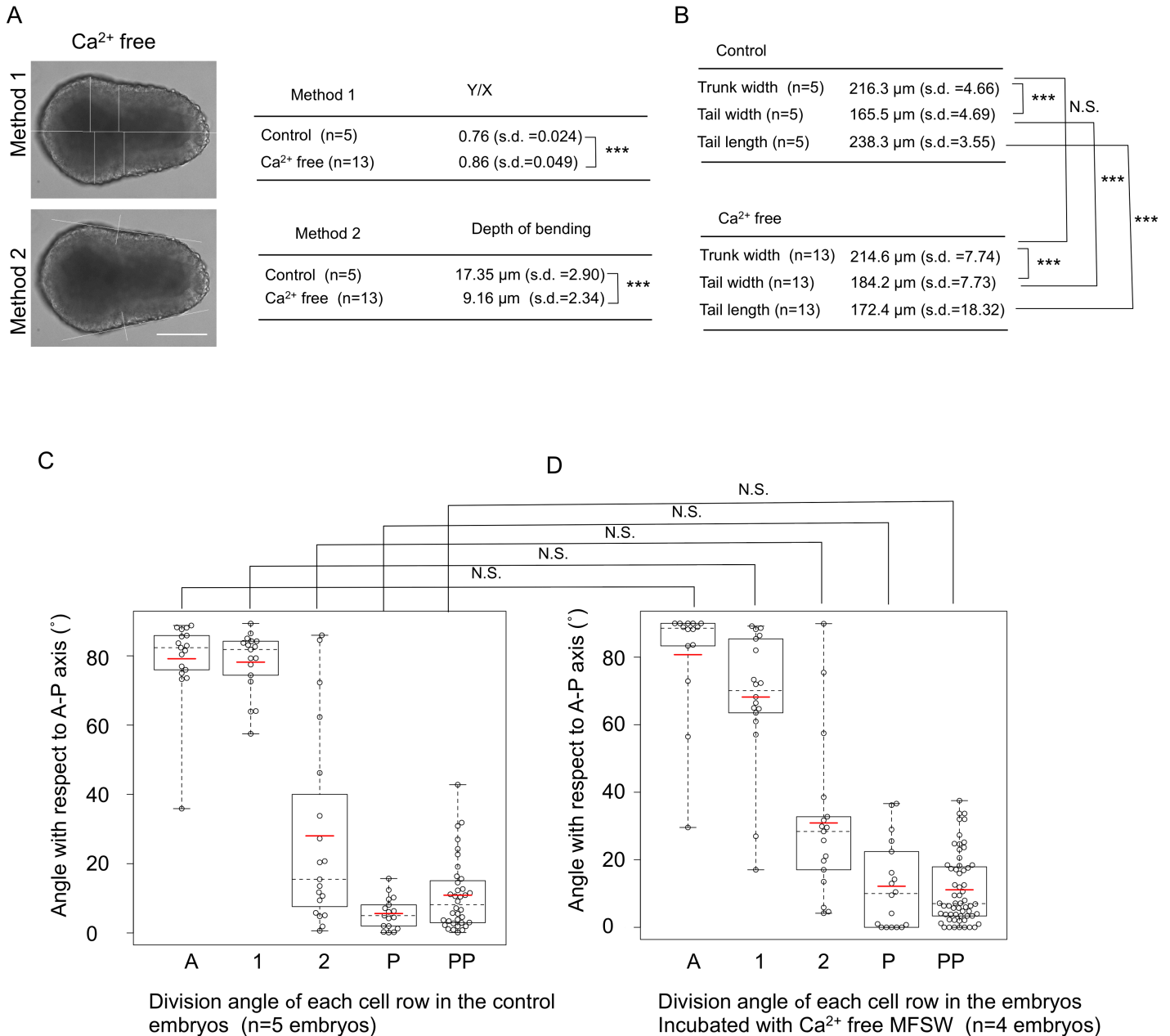
A

Ca²⁺ free

Method 1

Method 2

Method 1	Y/X
Control (n=5)	0.76 (s.d. =0.024)
Ca²⁺ free (n=13)	0.86 (s.d.=0.049)

***

Method 2	Depth of bending
Control (n=5)	17.35 µm (s.d. =2.90)
Ca²⁺ free (n=13)	9.16 µm (s.d.=2.34)

***

B

Control

Trunk width (n=5)	216.3 µm (s.d. =4.66)
Tail width (n=5)	165.5 µm (s.d.=4.69)
Tail length (n=5)	238.3 µm (s.d.=3.55)

*** N.S. *** ***

Ca²⁺ free

Trunk width (n=13)	214.6 µm (s.d. =7.74)
Tail width (n=13)	184.2 µm (s.d.=7.73)
Tail length (n=13)	172.4 µm (s.d.=18.32)

***

C

Angle with respect to A-P axis (°)

N.S. N.S. N.S. N.S. N.S.

A 1 2 P PP

Division angle of each cell row in the control embryos (n=5 embryos)

D

Angle with respect to A-P axis (°)

A 1 2 P PP

Division angle of each cell row in the embryos Incubated with Ca²⁺ free MFSW (n=4 embryos)

Figure S6 (related to Figure 6)
Effect of Ca2+ free sea water on the pattern of epidermal cell division and the formation of epithelial bending. (A) Phenotype of the embryo incubated in Ca2+ free sea water and quantitative evaluation of the epithelial bending. See experimental procedure for the calculation methods. Table shows the results of calculations. *** indicates $p<0.001$ (T-test). Scale bars, 100 µm. (B) The width of the trunk and tail regions and the tail length in the control embryos and the embryos incubated in Ca2+ free sea water. See experimental procedure for the calculation methods. N.S. and *** indicate $p>0.05$ and $p<0.001$, respectively (T-test). (C, D) Angle of division orientation with respect to the A–P axis in the control (C) and the embryos incubated in Ca2+ free sea water (D). The intact embryos (Fig. S5D) were used as the control. In the embryos incubated with Ca2+ free sea water (n=4 embryos), the values were extracted from 14 cells for row A, 18 cells for row 1, 17 cells for row 2, 18 cells for row P and 60 cells for row PP. Data are represented as individual values and boxplots. Means are indicated as red horizontal bars. Medians are indicated with dashed lines. Boxes indicate second and third quartiles, and whiskers indicate the maximum and minimum values. There is no statistically significant difference for each cell row between the intact control and the embryos incubated in Ca2+ free sea water. N.S. indicates $p>0.05$ (T-test).

TRANSPALENT METHODS

Animals and embryos

We obtained adults of *Halocynthia roretzi* from local fishermen near the Asamushi Research Center for Marine Biology (Aomori, Japan). Naturally-spawned eggs were fertilized using a suspension of nonself sperm. Embryos were cultured in Millipore-filtered seawater (MFSW) containing 50 µg/ml streptomycin and 50 µg/ml kanamycin at 9–13°C.

Constructs

This study used the following constructs: DCIC-EGFP: *Halocynthia roretzi* dynein cytoplasmic intermediate chain (DCIC) was identified in the MAGEST (EST database of eggs and embryos; http://magest.hgc.jp/) and Aniseed database (Harore.CG.MTP2014.S40.g04074, https://www.aniseed.cnrs.fr/). Based on the sequences of MAGEST contig 5549, which includes the 5'UTR, and the MAGEST contig 8626, which includes the 3'UTR, the entire ORF was cloned by RT-PCR using the forward primer (5'-GAAGGATCCACCATGTCAGAAAAATCTGATCGGAAAGCT-3') and reverse primer (5'-GAACCATGGTTAATTGTCTGGCTATCAATGCCTCTTCT-3'). Template cDNA was generated from the neurula stage mRNA. The fragments of DCIC and EGFP were inserted into pBSHTB(N). MAP7-GFP: MAP7-GFP in pSPE3 was a gift from Dr. Alex McDougall. The N-terminal fragment of mouse MAP7 was used (Prodon et al., 2010). H2B-GFP: H2B-GFP in pBSHTB(N) was a gift from Dr. Takehumi Negishi. MAP7-mCherry: N-terminal fragment of MAP7 from the MAP7-GFP in pSPE3 was inserted into the EAAARx3-mCherry in pBSHTB(N) (Takatori et al., 2010). PH-YFP: A PCR fragment containing PH-YFP from Tbx6b>PH-YFP (a gift from Dr. Anna DiGregorio) was inserted into the pBSHTB(N). PH-dTomato: PH-dTomato in pBSRN3 was a gift from Dr. Alex McDougall.

mRNA synthesis and microinjection

mRNAs encoding the fusion proteins (DCIC-EGFP, MAP7-GFP, MAP7-mCherry, H2B-GFP, PH-YFP, PH-dTomato) were synthesized *in vitro* using the mMessage mMachine kit (Ambion), and poly(A) was added to the 3' ends of the synthesized mRNAs using the Poly(A) Tailing kit (Ambion) according to the manufacturer's instructions. We used the following restriction enzymes and RNA polymerases: T3 and NotI for DCIC-EGFP; T3 and SfiI for MAP7-GFP; T3 and NotI for MAP7-mCherry; T3 and PstI for H2B-GFP; T3 and NotI for PH-YFP; and T3 and SfiI for PH-dTomato. The synthesized mRNA was microinjected into fertilized eggs, a4.2, b4.2, a7.15, or b7.15 cells according to Miya et al. (1997) and Niwano et al. (2009) as described in the following. Fertilized eggs were treated with 0.05% actinase E (Kaken Pharmaceutical, Japan) in MFSW for 10 min to remove the follicle cells on the chorion. The treated eggs were washed with MFSW and transferred on the cover glass in plastic petri dish filled with MFSW. The eggs with chorion but without follicle cells were stuck on the cover glass. The solution to be microinjected was loaded in glass needles for microinjection which were made by pulling glass capillaries (GDC-1, Narishige) with a horizontal puller (PN-3, Narishige). Microinjection was carried out with a micromanipulator (MN-151, Narishige) under the dissection microscope (OLYMPUS SZX16).

Live imaging

Time lapse observation was performed using either a LSM710 Zen zeiss confocal microscope (Fig. 1C, 3A, 3B, Supplemental Movies 2 and 3) or a Nikon eclipse T*i* (Fig. 2A, 4A, 5D, 6A, Supplemental Movies 1, 4–9). For observation with the LSM710 Zen zeiss confocal microscope, embryos with vitelline membrane were mounted on the slide glass in random orientations, and well-oriented embryos were selected for observation of their lateral sides. Images were obtained every 2 min at 1.0–2.5 µm intervals. For observation with the Nikon eclipse T*i*, the vitelline membranes were removed with forceps in a plastic dish coated with 1% agarose in MFSW. The embryos were transferred to a glass-bottomed dish (Matsunami) filled with 2% methylcellulose in MFSW and carefully oriented using tungsten needles so that the lateral side could be observed. Images were obtained every 2–4 min at 4.0 µm intervals and were then subjected to deconvolution with the Nikon NIS-Elements software to reduce blurriness. The two different methods revealed the same pattern of epidermal cell divisions.

Drug treatment

Dynein inhibitor Ciliobrevin D (Calbiochem) was dissolved in DMSO at 50 mM and stored at −20°C

as a stock solution. Before use, the stock solution was diluted to 30 µM in MFSW. The embryos were treated with 30 µM Ciliobrevin D for 1 h, beginning 1 h after neurula rotation (NR) (approximately 30 min before the 11th epidermal cell divisions). In another experiment, embryos were treated with 10 µM Ciliobrevin D for 2 h, beginning 1 h after NR. Following the treatment, embryos were washed with MFSW and then either used for live-imaging, as described above, or placed under the dissection microscope (OLYMPUS SZX16) to observe the epithelial bending. The 11th cell divisions had not begun at the time of washing with MFSW. The control embryos were treated with 0.4% DMSO for 1h from the NR+1 h stage. Another dynein inhibitor, EHNA (Santa Cruz Biotechnology), was dissolved in sterilized water at 50 mM and stored at 4°C as a stock solution. Before use, the stock solution was diluted in MFSW to either 1 mM or 2 mM. At 1 h after NR, the embryos were treated with 2 mM EHNA for 1 h and then treated with 1 mM EHNA for another 30 min. The treated embryos were washed with MFSW and used for live-imaging, as described above. Hydroxyurea (HU) (Sigma) was dissolved in MFSW at 20 mM, 50 mM and 100 mM.

Definition of the start and the end of the 11th cell division
When epidermal cells begin to divide, the surface of the embryo becomes rough due to the formation of division furrows. This can be detected by the dissection microscope (OLYMPUS SZX16) and is defined as the onset of the 11th cell division. The surface of the embryo becomes smooth upon completion of epidermal cell divisions. This can also be detected by the dissection microscope and is defined as the end of the 11th cell division.

Immunohistochemistry and Phallacidin staining
For anti-dynein antibody staining, embryos were fixed in ice-cold methanol for 10 min and washed four times with 0.1% Triton X-100 in PBS (PBSTr). The fixed embryos were treated with 3% H_2O_2 in PBS for 10 min and with 50 mM NH_4Cl in PBS for 15 min. After being washed with PBS four times, the specimens were incubated for 30 min at room temperature with 0.5% blocking reagent (Roche) in PBS. Anti-dynein heavy chain antibody (R-325, Santa Cruz Biotechnology) was diluted at 1:50 in 0.5% blocking reagents in PBS, and the specimens were incubated overnight at 4°C. The primary antibody was washed with PBSTr four times. We used the MaxPO system (Nichirei Corporation) as a secondary antibody. Anti-rabbit antibody conjugated with HRP [MAX-PO (R)] was diluted at 1:20 in 0.5% blocking reagents in PBS, and the specimens were incubated overnight at 4°C. The secondary antibody was washed four times with PBSTr, and HRP activity was detected using the TSA Plus Cy3 kit (Perkin–Elmer Life Sciences) according to the manufacturer's instruction.
 To identify the lineage boundary, H2B-GFP mRNA was injected into the b4.2 cell at the 8-cell stage, and the embryos were fixed as described above. The fixed embryos were double stained with anti-dynein heavy chain antibody and anti-GFP antibody (ab13970, Abcam), as described above, with the following exception: anti-GFP antibody was diluted at 1:200 in 0.5% blocking reagents in PBS. As a secondary antibody, anti-chicken Alexa 488 antibody (A11039, Invitrogen) was diluted at 1:100 in 0.5% blocking reagents in PBS.
 To determine which side of the cell was enriched with dynein protein, specimens were squished gently to separate the cells, and cell boundaries were identified using the differential interference contrast (DIC) optics of the Zeiss LSM5 PASCAL confocal microscope.
 For Phallacidin (Thermo Fisher Scientific) staining, embryos were fixed for 30 min in 4% paraformaldehyde in a buffer containing 50 mM EGTA, 100 mM Pipes and 400 mM sucrose, adjusted to pH 6.9 (Munro and Odell, 2002a). The fixed embryos were washed three times with PBS and incubated with Phallicidin (5 unit/ml) in PBSTr either for 1 h at room temperature or overnight at 4°C and then washed three times with PBS. The embryos were treated with isopropanol series (70%, 85%, 95% and 100% in PBS) for 1 min each, and cleared with Murray clear (Benzyl Benzoate:Benzyl Alcohol = 2:1). The specimens were observed using the Zeiss LSM5 PASCAL confocal microscope.

Isolation of epidermal cell sheet
The vitelline membrane was removed manually using forceps, and the embryos were transferred to plastic dish coated with 1% agarose in MFSW. Embryos were dissected along the midline using an eyebrow hair mounted on the tip of a glass needle. Either the left side half or the right side half was used. The tissues underlying muscle and notochord cells were identified by their large cell size and cell shape. For removal of the dorsal and ventral regions, the locations of the muscle and notochord cells were employed as landmarks of the lateral region. After the removal of dorsal and ventral epidermal cells, the underlying muscle and notochord cells were removed gently with the eyebrow hair. The isolated ectodermal cell sheets were transferred gently to 2% methylcellulose in MFSW and the pattern of division was observed using the Nikon eclipse T*i*, as described above.

Image analyses and measurements
The pattern of epidermal cell division was characterized using Image J software. The A–P axis was defined as the farthest two points of the lateral side of the embryos. The long axis and short axis of cells were measured based on the best-fit ellipse using the measurement tool in Image J. The axis of division orientation (Fig. 2C) was defined as one line perpendicular to the division plane immediately on recognition of the division plane. Angles between axes, such as the A–P axis and division orientation (Fig. 2C), were measured using the angle measurement tool in Image J.

To quantify the width of the trunk and tail regions and the tail length before and after epithelial bending formation, images were obtained, in which embryos were oriented either dorsal or ventral up. Lines were drawn perpendicular to the midline at all level from anterior to posterior. Positions along the A–P axis were determined where the lines from the lateral end of the embryo to the midline were longest in the trunk and tail regions, and the lengths were defined as either width "a" for trunk or "b" for tail (Fig. 4F). Another line was drawn either coinciding with the epidermal A–P boundary visualized by a fluorescent protein injected into b4.2 in the embryo before bending formation or by connecting the deepest points of the epithelial bending on the both sides of the embryo. The length from the intersection between this line and midline to the posterior end was defined as tail length (indicated as "c" in Fig. 4F).

Two methods were used to calculate the extent of the epithelial bending. In the first method, an image was obtained in which the area of the embryo was at its maximum. Lines were drawn perpendicular to the midline at all levels from anterior to posterior (Fig. 4D, top). Positions along the A–P axis were determined where the lines from the lateral end of the embryo to the midline were either longest in the trunk region or shortest in the boundary between the trunk and tail regions, and the lengths were defined as either X or Y (Fig. 4D, top). The extent of the epithelial bending was calculated as Y/X. In the second method, a tangential line that was in contact with the trunk and tail surfaces was drawn on either lateral side of the embryo (Fig. 4D, bottom). Lines perpendicular to the tangential lines were drawn between the contact points, and the line furthest from the tangential line on the lateral side of the embryo was used to measure the extent of the epithelial bending.

To characterize the convergent extension of the notochord, embryos were stained with Phallacidin, as described above, and observed using the confocal microscope LSM5 PASCAL (Zeiss). The notochord was outlined using the polygon selection tool (Fig. 6C). A rectangle was drawn whereby each line touched the outline of the notochord. The aspect ratio of the notochord was measured as the length/width of the rectangle. A single z-section, where the aspect ratio was the maximum among other z-series, was used.

To quantify the anterior enrichment of dynein protein, the center of the cell was determined by the centroid tool in Image J (red in Fig. 5B). Three lines intersecting on the cell center were drawn: a reference axis (blue dotted lines in Fig. 5B) runs in the A-P direction; the other two with angles of 20˚ with respect to the reference axis on the both sides (fig. 5B). The signal intensity of the anterior and posterior surfaces of the cell (0.5 µm thickness) within the range between -20˚ and 20˚ was measured. The ratio of the anterior to the posterior intensities was calculated for each cell.

To quantify the fluorescent signals of DCIC-EGFP and PH-dTomato in the surface of the cells, the surface area in which the signal intensity is measured was determined as described earlier (the range between -20° and 20°). The RGB profiler tool in Image J was then used to measure the signal intensity within the determined width in all pixels from anterior to posterior approximately 2.7 µm (8 pixels) into the cell on either side of the peak of the PH-dToamato signal (Fig. 5C4). Average signal intensities of DCIC-EGFP and PH-dTomato from 26 different cell boundaries were calculated for each pixel.

Supplemental References
Miya, T., Morita, K., Suzuki, A., Ueno, N., Satoh, N., 1997. Functional analysis of an ascidian homologue of vertebrate Bmp-2/Bmp-4 suggests its role in the inhibition of neural fate specification. Development *124*, 5149–5159.
Niwano, T., Takatori, N., Kumano, G., Nishida, H., 2009. Wnt5 is required for notochord cell intercalation in the ascidian Halocynthia roretzi. Biol. Cell *101*, 645–659.
Takatori, N., Kumano, G., Saiga, H., Nishida, H., 2010. Segregation of germ layer fates by nuclear migration-dependent localization of not mRNA. Dev. Cell *19*, 589–598.